Computational finite element modeling of stress-state- and strain-rate-dependent failure behavior of ceramics with experimental validation

Zahra Zaiemyekeh[a,*], Haoyang Li[a], Saman Sayahlatifi[a], Min Ji[a], Jie Zheng[a], Dan L. Romanyk[a], James D. Hogan[a]

[a] *Department of Mechanical Engineering, University of Alberta, Edmonton, AB T6G 2R3, Canada*

Abstract

This study investigates the stress-state- and strain-rate-dependent behavior of CeramTec ALOTEC 98% alumina (Al_2O_3) ceramic through experimentally validated finite element (FE) modeling. As the constitutive material model, a rate-dependent viscosity-regularized phenomenological model (JH2-V model) was implemented through a VUMAT subroutine in ABAQUS software. The FE model was informed and validated with the data for indirect tension and compression-shear tests under dynamic rates both quantitatively (i.e., stress-strain histories and lateral strain-axial strain curves) and qualitatively (i.e., manifestation and accumulation of damage). The validated model was leveraged to study the effect of the JH2-V model regularization parameters, mesh sensitivity, and bulking across different stress states. Additionally, by modeling the compression-shear specimen with different angles, the effect of shear on the material response was quantitatively investigated through the definition of a volumetric average damage parameter and shear strain history. Altogether, the outcomes of this study have implications for the computational design and development of ceramic-based structures in higher-scale applications (e.g., impact).

Keywords: Alumina (Al_2O_3) ceramic, Finite element modeling (FEM), Dynamic behavior, Indirect tension experiments, Compression-Shear experiments

[*] Corresponding author
Email address: zaiemyek@ualberta.ca (Zahra Zaiemyekeh)

1. Introduction

Advanced ceramics have a wide range of applications (e.g., protection [1, 2] and aerospace [3, 4]) owing to their desirable mechanical properties, such as low density [5, 6], high compressive strength [7, 8], and high hardness [9, 10]. Under loading, the damage evolution in ceramics is a complex phenomenon involving various spatially and temporally evolving mechanical responses and deformation mechanisms, particularly at higher strain rates [11, 12]. To optimize the performance of advanced ceramics, it is important to consider the role of stress-state- and strain-rate-dependent behavior to better capture their failure phenomena [13, 14]. This study focuses on the alumina (Al_2O_3) ceramics due to the cost-benefit ratio relative to other ceramics (e.g., boron carbide) [6, 15] to provide a comprehensive investigation of the stress-state- and strain-rate-dependent behavior of the material through a combined experimental and numerical approach.

In the literature, the behavior of alumina ceramics has been mainly explored under uniaxial compressive loading for both quasi-static and dynamic strain rates [16–26]. For example, Lo et al. [26] performed quasi-static and dynamic uniaxial compression tests to characterize the mechanical response of an AD85 alumina ceramic. They found that variability in the mechanical properties was larger at quasi-static conditions compared to dynamic, and this is attributable to the activation of a higher number of pores at higher loading rates. In another study, the dynamic macro-cracking and fragmentation process of alumina under uniaxial compression was studied by Wang et al. [6]. It was found that the compressive strength of alumina is almost insensitive to the low strain rate regimes, while it is significantly sensitive to higher strain rates ($\geq 250\ \mathrm{s}^{-1}$). In contrast to many experimental studies exploring the uniaxial compressive behavior of alumina ceramics, limited efforts have been made to address the dynamic response of the material under tensile [27, 28] and combined loading conditions [29–31], where the effects of the stress state and loading rate on the mechanical properties and fracture mechanisms remain a field of interest. In this study, we seek to study the indirect tension and compression-shear response of Al_2O_3 ceramics to reveal the effect of stress state on failure response of the material.

To investigate the tensile and combined loading behavior of advanced ceramics, different methods have been proposed. The Brazilian disk (BD) [28, 32, 33] and the modified flattened Brazilian disk (FBD) [27, 34] experiments have been used in multiple studies as a typical indirect tension test to determine the tensile strength of brittle materials such as ceramics [27, 32] and rocks [35, 36]. To explore the shear-dominated behavior of brittle solids, hydraulic confinement techniques [37–39] and inclined specimen methods with a modified split-Hopkinson Pressure Bar (SHPB) system [40–42] have been employed in the previous studies. In a study by Du et al. [43], oblique cylindrical rock specimens with varying hydrostatic confining pressures were tested under different loading rates, and they found that by increasing the specimen inclination angle and the hydrostatic confining pressure, the failure pattern of the specimens changed from the tensile-dominated failure to shear-dominated failure. In a separate study by Xu et al. [40], angled rock specimens were used in the SHPB setup to achieve a combined compression-shear stress state, and it was found that all the inclined specimens exhibited a prominent shear-dominated failure accompanied by localized tensile damage. Based on previous studies [28, 32, 41, 42], the FBD and angled specimen are adopted in the current study to investigate the rate-dependent tensile and compression-shear responses of the Al_2O_3 ceramics.

In addition to the experimental efforts, various constitutive models have been proposed to capture/describe the mechanical response of ceramic materials to obtain higher spatial and temporal resolutions. These models include phenomenological models (e.g., Johnson–Holmquist-I (JH1) [44], Johnson–Holmquist-II (JH2) [45], Johnson-Holmquist-Beissel (JHB) [46], Simha et al. [47], and Simons et al. [48, 49]), and mechanism-based material models (e.g., models by Rajendran and Grove [50, 51], Deshpande and Evans [52, 53], and Paliwal and Ramesh [54]). Among the phenomenological material models, the model developed by Johnson-Holmquist (i.e., JH2) [45], as a pressure dependent plasticity model, has been widely used to predict the response of ceramics under high strain rate loading conditions because of simplicity in implementation and applicability to a wide range of tests [12, 15, 55]. However, in a study by Simons et al. [48] indicated that damage initiation and propagation could be affected due to strain localization upon failure which is related to mesh characteristics in softening plasticity models (e.g., JH2 model). To improve the JH2 material model, Simons et al. [48, 49] proposed a regularized viscosity JH2 model (JH2-V). In the JH2-V model, the hydrostatic tensile strength was formulated as a function of the rate of equivalent plastic strain and a viscosity parameter to account for the strain-rate-dependent spall (hydrostatic tensile) strength of ceramics. This rate-dependent definition of tensile strength leads to a rate-dependent yield surface that helps to reduce strain localization [48, 56]. In addition, the fracture strain formulation was revised in the Simons et al. [49, 57] studies by defining pressure-dependent transition points to better capture the asymmetry in the rate of damage growth under tension and compression [49].

Motivated by previous efforts, this study investigates the stress-state- and strain-rate-dependent behavior of alumina ceramics under tensile and combined compression-shear stress states through an experimentally validated finite element (FE) framework with the JH2-V model incorporated. Experimentally, the effect of stress state on failure response of alumina ceramics is explored by designing and testing angled specimens to induce a compression-shear stress state and FBD specimens to induce a tensile stress state in the material. The mechanical testing is carried out using a SHPB setup for dynamic strain rates in conjunction with ultra-high-speed imaging and digital image correlation (DIC). Computationally, the JH2-V model is implemented in ABAQUS software by using a VUMAT subroutine and is validated with experimental data. Once validated, the model is exercised to quantitatively analyze the damage initiation and growth with the presence of shear loading, and providing guidance for higher scale (e.g., impact events) in terms of element size selection. Ultimately, the outcomes of this study provide insights into the role of stress state (e.g., the presence of shear) on the failure response of Al_2O_3 ceramics that is applicable to the design of ceramic structures in a range of applications (e.g., impact [58, 59], and aerospace [4, 60]).

2. Experimental Methodology

In this study, commercially available 98% purity alumina (Al_2O_3) from CeramTec, Germany, with a manufacturer-specified density of 3.9 g/cm^3, Young's modulus of 380 GPa, Poisson's ratio of 0.22, fracture toughness of 3.5 MPa $\sqrt{m}$, bending strength of 260 MPa, and average grain size of $\sim$ 1.85 μm was studied. For dynamic compression-shear experiments, cuboidal specimens with nominal dimensions of 3.5 mm $\times$ 2.3 mm $\times$ 2.7 mm, and a tilting angle of 5° were used. For indirect tension experiments, the FBD specimens with a diameter of 8 mm and thickness of 4 mm were fabricated. Figure 1 (a) and (b) shows the dimension and geometry of the specimens. In the FBD specimens, to facilitate the formation of a central crack and reduce shear strain, the thickness-to-diameter ratio was set to be 0.5 [27, 61], and two parallel flat ends were introduced to the specimen to reduce stress concentrations [61, 62]. The FBD samples used in this numerical study were fabricated based on the geometrical guidelines provided in the literature [63, 64] to increase the likelihood of the initiation of a central crack and a successful FBD experiment [64]. In addition, a loading angle (i.e., 2α) is selected to be 20° following Griffith strength theory [65] to allow crack initiation at the center of the disk, and this loading angle was also used in previous studies [61, 65].

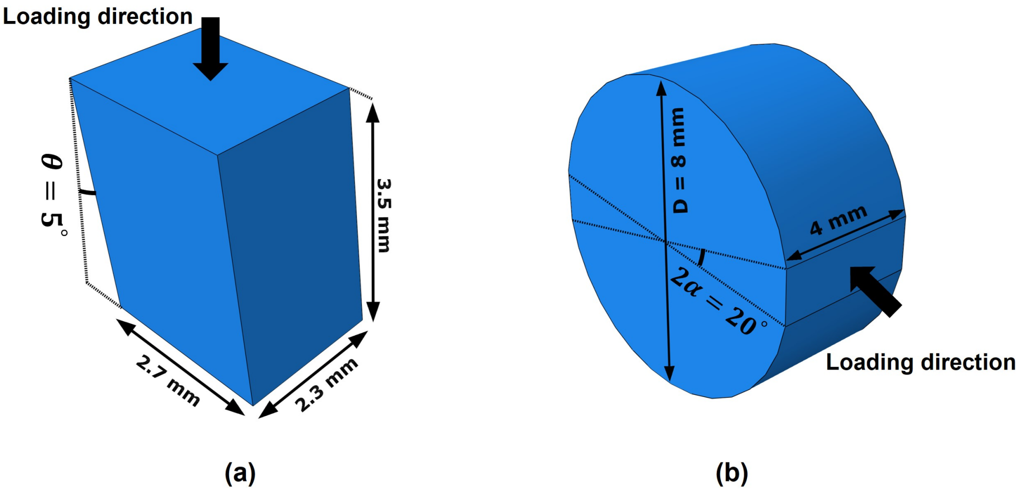

Figure 1: (a) The geometry and dimensions of the angled ($\theta = 5°$) ceramic specimens designed to induce a compression-shear stress state in the material, and (b) The geometry and dimensions of the FBD ceramic specimens with flattened surfaces defined by 2α =20° designed to induce a tensile stress state in the material.

2.1 Material Characterization

In the current study, the scanning electron microscopy (SEM) of the polished surface (mechanically polished down to 0.25 μm) of the as-received CeramTec 98% alumina ceramic coupled with an energy dispersive x-ray spectroscopy (EDS) was conducted to characterize the typical microstructure and the elemental composition of the material. Shown in Fig. 2 (a) is an SEM image of the material which is obtained using a Zeiss Sigma FESEM machine. Fig. 2 (b to f) shows the EDS map data which is post-processed using the Aztec software from Oxford Instruments. As seen, the alumina ceramic in this study is mainly composed of oxygen (weight and atomic percentages are 56.86% and 69.05%, respectively) and aluminum (weight and atomic percentage are 41.75% and 30.06%, respectively) mixed with traces of Mg, Si, and Ca which are the consequence of fabrication process [66].

2.2 Mechanical Testing Set up

The dynamic indirect tension and compression-shear tests were conducted on a modified split-Hopkinson pressure bar (SHPB). The diameter of the incident and transmission bars was 12.7 mm with lengths of 1016 mm and 914 mm, respectively. The bars were made of hardened maraging steel (Service Steel America C-350) with density, elastic modulus, yield strength, and Poisson's ratio of 8080 kg/m^3, 200 GPa, 2.68 GPa, and 0.29, respectively. Shown in Fig. 3 is a schematic of the SHPB experimental setup. Two impedance-matched Ti-6Al-4V titanium alloy jacketed tungsten carbide (WC) platens with diameters the same as the bars were attached to the

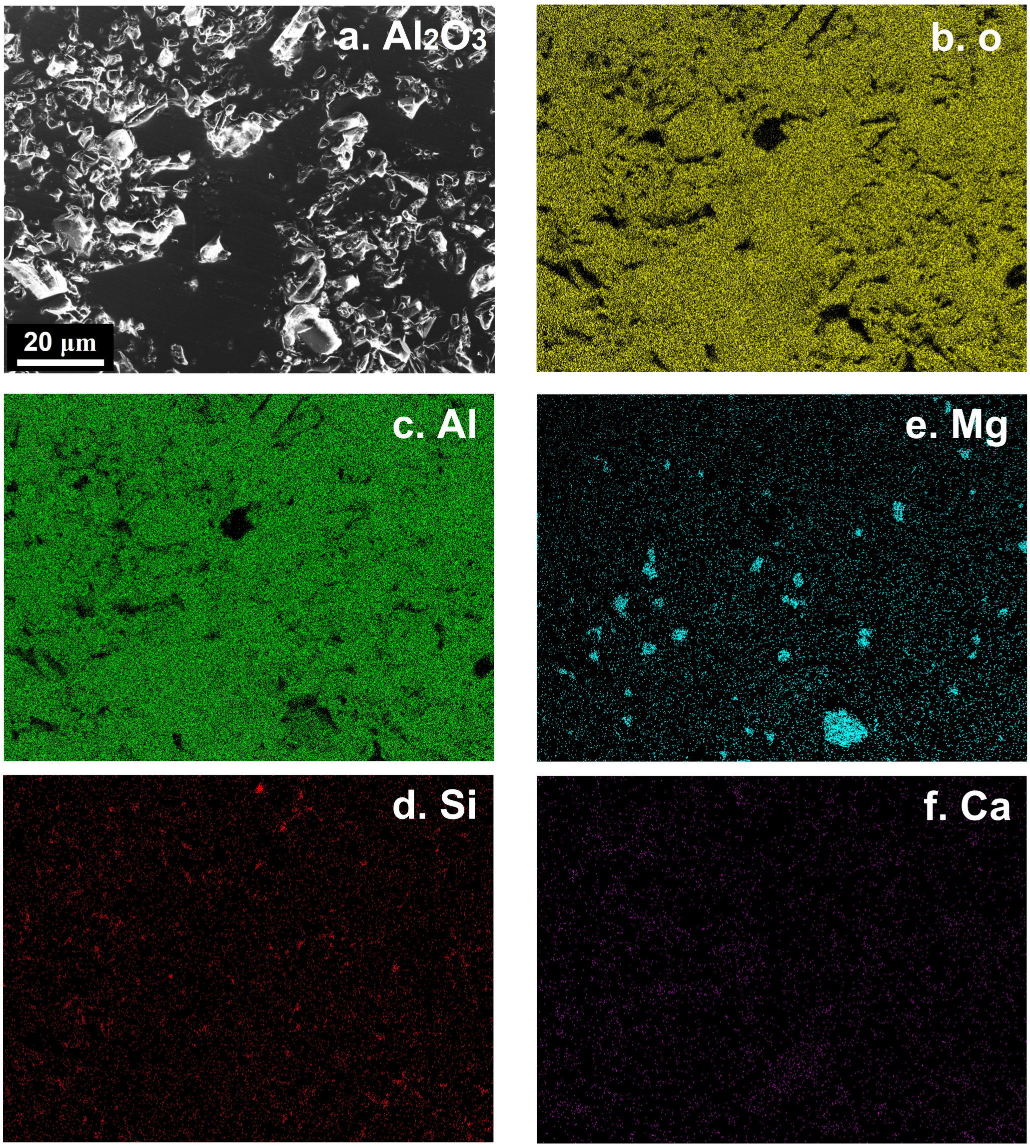

Figure 2: SEM micrograph examining the microstructural features of the as-received material and EDS concentration mapping shows the distributions of selected elements. (a) SEM image of CeramTec alumina with 98 wt.% purity. (b) The distribution and concentration of O (atomic 69.05%, weight 56.86%) in the SEM image, show that it is present everywhere except for the dark spots. (c) Distribution and concentration of Al (atomic 30.6%, weight 41.75%) in the SEM image. (d) Distribution and concentration of Mg (atomic 0.43%, weight 0.35%). (e) Distribution and concentration of Si (atomic 0.3%, weight 0.43%). (f) Distribution and concentration of Ca (atomic 0.24%, weight 0.51%)

.

end of the incident and transmission bar to aid in re-distributing the loads, prevent indentation, and reduce stress concentration on the specimen. This setup has been used previously, and the results have been published [66, 67].

In the indirect tension experiments, the thicker specimen may lead to a secondary contact

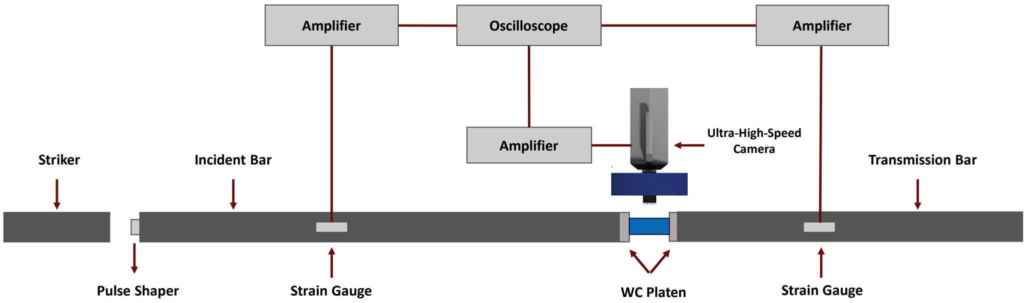

Figure 3: The split-Hopkinson Pressure Bar (SHPB) experimental setup.

with the loading platens upon fracture, and this may result in the manifestation of a second peak on the recorded history of stress [27]. To avoid such an effect, no protection platens were used in the indirect tension tests. It is also worth noting that in the indirect tension experiments, the specimen was placed between the bars lubricated with high-pressure grease to reduce the frictional effect during loading, while in compression-shear tests no grease lubrication was applied to promote sufficient friction for shearing. In this SHPB setup, the data was collected with two strain gauges (Micro 184 Measurements CEA- 13–250UN-350) attached to the bars. For the uniaxial compression-shear experiments, the transmission strain gauge signal, $\epsilon_t(t)$, was used to calculated the stress-time response $\sigma(t)$ [68]:

$$\sigma(t) = \frac{A_0}{A_s} E_0 \epsilon_t(t), \tag{1}$$

here, A_0 (m^2) and A_s (m^2) are the cross-sectional areas of the bar, and specimen, respectively; $\epsilon_t(t)$ is the transmitted strain-time history, and E_0 (N/m^2) is the elastic modulus of the bar material. For the indirect tension experiments, the tensile stress is calculated using the elasticity theory [69]:

$$\sigma_\theta = K \frac{2P}{\pi D t}, \tag{2}$$

where P, D, and t are the loading force applied to the specimen, diameter, and thickness of the disk, respectively. Here, K is a dimension coefficient as a function of the loading angle (i.e., 2α) of the flattened disk [70]. If $2\alpha = 0^\circ$ (i.e., coventional Brazilian disk), K is equal to 1, and if $2\alpha = 20^\circ$, K is approximated to 0.95 [69, 70].

In the dynamic experiments, pulse shapers were placed in front of the incident bar to provide a ramped signal, where the ramp pulse shape helps the ceramic specimen achieve stress equilibrium and constant strain rate during the high strain rate testing, as well as to filter the highfrequency component of the incident pulse [71, 72]. The indirect tension and compression-shear tests were conducted at strain rates ranging from 10 to 170 s^{-1} and 70 to 800 s^{-1}, respectively, through modifying the pulse shapers, and striker length. Table 1 summarizes the pulse shapers and lengths of strikers used in this study. To monitor the displacement and strain maps of the specimen during the experiments and to better visualize crack initiation and propagation, a Shimadzu HPV-X2 ultra-high-speed (UHS) camera images of speckled specimens coupled with DIC (VIC-2D V6, Correlated Solutions, Irmo, South Carolina, USA). The DIC analysis process used here follows that used in previous work, and the reader may refer to [27, 29] for further specific details. The stress-strain curves were obtained by combining the average strain (the average strain was calculated by averaging across the area of interest (AOI) in the DIC analysis) profile with the stress profile generated from the data recorded by the strain gauge on the transmission bar by using Eq. (1) and Eq. (2). Lateral strain-axial strain curves were also generated using the DIC measurements.

Table 1: Pulse shaping characteristics used in dynamic loading (all dimensions are in mm).

Compression-shear experiments

Strain rate (s^{-1})	Material	Pulse shaper diameter	Thickness	Striker length
70 to 100	Tin	3.97	1.58	300
300 to 450	Thin HDPE	3.18	1.58	300
450 to 800	Thick HDPE	3.18	2.38	125

Indirect tension experiments

Strain rate (s^{-1})	Material	Pulse shaper diameter	Thickness	Striker length
10 to 20	Tin	3.97	1.58	300
25 to 40	Thin HDPE	3.97	1.58	300
90 to 170	Paper	3.97	0.5	125

Note. HDPE is the abbreviation for high-density polyethylene.

3. Numerical Methodology

In this section, the theoretical framework of the JH2-V material model is first outlined, and the corresponding constants used in this study are given (Table 2). Next, the FE model of the SHPB setup is described to explore the behavior of Al_2O_3 ceramics under indirect tension and compression-shear stress states.

In the JH2-V model, as the first modification to the JH2 material model to accommodate the strain localization, the hydrostatic tensile strength was formulated as a function of the rate of equivalent plastic strain ($\dot{\epsilon}_P$) and a viscosity parameter (η). This strain-rate-dependent definition of tensile strength led to a strain-rate-dependent yield function. In the JH2-V model, the strength is defined as an analytical functions of pressure and other parameters as [45, 48]:

$$\sigma^* = \sigma_i^* - D\left(\sigma_i^* - \sigma_f^*\right) \tag{3}$$

$$\sigma_i^* = A\left(P^* + T^*(\dot{\epsilon}_P)\right)^N \tag{4}$$

$$\sigma_f^* = B\left(P^*\right)^M \tag{5}$$

where σ^* is the normalized strength of the material, σ_i^* shows the normalized intact strength, σ_f^* represents the normalized fracture strength, D is the damage variable with a value between 0 and 1, A and N are intact strength constants, and B and M are fracture strength constants. Here, $\sigma^* = \frac{\sigma}{\sigma_{HEL}}$, $P^* = \frac{P}{P_{HEL}}$, $T^* = \frac{T}{P_{HEL}}$, and $\dot{\epsilon}^* = \frac{\dot{\epsilon}}{\dot{\epsilon}_0}$, where σ, σ_{HEL}, P, P_{HEL}, T, and $\dot{\epsilon}_P = \dot{\gamma}$ are the equivalent stress, equivalent stress at the Hugoniot elastic limit (HEL), actual hydrostatic pressure, pressure at the HEL, maximum tensile hydrostatic pressure tolerated by the material, and rate of the equivalent plastic strain, respectively.

Then, the hydrostatic tensile pressure $T(\dot{\epsilon}_p)$ is defined as a mixed linear/logarithmic formulation [48]:

$$T(\dot{\epsilon}_p) = T(\dot{\lambda}) = \begin{cases} T_0 + \eta\dot{\lambda}, & \text{for } \dot{\lambda} < \dot{\lambda}_t \\ T_t(1 + \frac{\eta\dot{\lambda}_t}{T_t}(\ln \dot{\lambda}/\dot{\lambda}_t)), & \text{for } else \end{cases} \tag{6}$$

here, η is the viscosity constant, $\dot{\lambda}$ represents the rate of plastic multiplier, T_0 is the reference rate-independent tensile strength parameter, T_t is a transition pressure ($T_t = T_0 + \eta\dot{\lambda}_t$), and $\dot{\lambda}_t$ represents the threshold rate for switching from the linear equation to logarithmic equation. Simons et al. [49, 57] found that by using linear equation, the failure zone size in impact simulations increased rapidly with increasing loading rate, which is physically unrealistic. The logarithmic formulation is used to eliminate the rapid increase in the failure zone at high rate loading (i.e., $\dot{\lambda} \geq \dot{\lambda}_t$).

In addition, in the JH2-V model, the damage starts to accumulate once the yield function is met as shown in Eq. (7). The damage value is calculated based on incremental equivalent plastic strain accumulation ($\Delta\epsilon_p^{eff}$), as shown in Eq. (8):

$$\emptyset(\sigma, D, \dot{\lambda}) = \sigma_q - \sigma_{HEL}\sigma^* \tag{7}$$

$$D = \sum \frac{\Delta\epsilon_p^{eff}}{\epsilon_p^f} \tag{8}$$

where σ_q is the von Mises stress, and ϵ_p^f is the equivalent fracture plastic strain, which is defined by the tri-linear equivalent plastic strain formulation [49]:

$$\epsilon_p^f = \begin{cases} \epsilon_p^{min}, & p < p_t \\ \frac{p(\sigma)-p(t)}{p(c)-p(t)}(\epsilon_p^{max} - \epsilon_p^{min}) + \epsilon_p^{min}, & p_t < p < p_c, \ and \\ \epsilon_p^{max}, & p_c < p \end{cases} \tag{9}$$

here, for pressures below p_t and above p_c, a fixed minimum failure strain (ϵ_p^{min}) and a fixed maximum failure strain (ϵ_p^{max}) is assumed. For intermediate pressure values, the fracture strain is defined through linear interpolation. This formulation allows for independent control of damage rate under tensile and compressive loading [49, 57], which requires data (i.e., p_t, p_c, ϵ_p^{min}, and ϵ_p^{max}) on the transition points from a brittle to inelastic response of ceramics. Ceramic materials exhibit a brittle failure behavior under tension, and show inelastic deformation under high confining pressures [72]. Such inelastic deformation mechanisms have been also observed in brittle solids under shock compression [73–75]. This new formulation (Eq. (9)) allows to better account for such phenomena.

Lastly, to calculate pressure, a polynomial equation of state (EOS) represented by the relationship between hydrostatic pressure (P) and volumetric strain (μ) is defined as per Eq. (10) [45]. As the damage starts to accumulate, bulking manifests as an incremental pressure (ΔP) added to the EOS that is defined as per Eq. (11) [45, 76]. The value of ΔP varies from 0 when $D = 0$ to $\Delta P = \Delta P_{max}$ when $D = 1$. In this study, ΔP is calculated based on the conversion of internal elastic energy to potential internal energy owing to the decrease in shear and deviator stresses [45]:

$$P = \begin{cases} K_1\mu + K_2\mu^2 + K_3\mu^3 + \Delta P, & \text{if } \mu > 0 \\ K_1\mu, & \text{if } \mu \leq 0 \end{cases} \tag{10}$$

$$\Delta P_{t+\Delta t} = -K_1\mu_{t+\Delta t} + \sqrt{(K_1\mu_{t+\Delta t} + \Delta P_t)^2 + 2\mu K_1 \Delta U} \tag{11}$$

$$\Delta U = U_t - U_{t+\Delta t} \tag{12}$$

$$U = \frac{\sigma_y^2}{6G} \tag{13}$$

where K_1 is the bulk modulus, K_2 and K_3 represent EOS constants, and μ is the volumetric strain. The internal elastic energy is shown by U which is related to the equivalent plastic flow stress σ_y, the fraction of the elastic energy loss converted to potential hydrostatic energy is β, and G is the shear modulus. The elastic constants G and K, Young's modulus and Poisson's ratio were measured from the experimental stress-strain and lateral strain-axial strain curves (see Fig. 7), and then G and K were calculated with the theoretical relations between the elastic constants. The calibrated constants are the regularization parameters, including η and $\dot{\lambda}_t$. These parameters were changed within their feasible range proposed by Simons et al. [48, 49] to obtain the best match with the experimental stress-time curves and the pattern of damage initiation and propagation observed in ultra-high-speed camera images. The effect of these parameters is studied in detail in Fig. 8 and Fig. 9.

Summarized in Table 2 are the material constants of Al_2O_3 ceramic for the JH2-V model, which are mainly calibrated or obtained from previous studies [49, 77] and experiments in this current study. The model was implemented into ABAQUS via a VUMAT subroutine. For more details on the implementation of the JH2-V model, the reader is referred to Appendix A.

3.1 Model Description

In this study, the FE model was constructed for the entirety of the SHPB system, including the bars, the loading platens, and the specimens (see Section 2). The time step was set at 400 μs. The general contact algorithm was used where frictionless surface-to-surface contact was defined between the potential contacting surfaces of the FBD sample and the platen, given that these interfaces were lubricated in experiments to avoid inducing complex stress states. The same contact modeling approach was applied to the compression-shear model, but a coefficient of friction of 0.06 [6] was considered for the interfaces between the sample and platens as no lubrication was applied in experiments to induce more tangential force and avoid surface sliding between the specimen and platens. To apply the load (see Fig. 4 (a)), the experimentally

Table 2: The JH2-V constants used for Al_2O_3 ceramics.

Parameter	Value	Unit	Source
A	0.93	-	[77]
B	0.31	-	[77]
N	0.6	-	[77]
M	0.6	-	[77]
K_1	226	GPa	Current study
K_2	0	GPa	[77]
K_3	0	GPa	[77]
ρ	3900	kg/m^3	Current study
G	155	GPa	Current study
T	0.2	GPa	[49]
HEL	6.25	GPa	[49]
P_{HEL}	7.5	GPa	[49]
β	1	-	[49]
η	0.025	MPa·s	Calibrated in the current study
$\dot{\lambda}_t$	10000	s^{-1}	Calibrated in the current study
ϵ_p^{max}	0.496	-	[49]
ϵ_p^{min}	$1.5.10^{-4}$	-	[49]
p_c	3.02	GPa	[49]
p_t	-0.17	GPa	[49]

measured pressure pulse was applied on the cross-section of the modeled incident bar where the strain gauge was placed in the experiments. Fig. 4 (b) shows the pressure pulse that was experimentally recorded through the strain gauge mounted on the incident bar; this pulse was used as the input to the model to induce the strain rate in the specimen. Shown in Fig. 4 (c) and (d) are the alignment of the FBD and angled specimens between the modeled bars and the WC platens, respectively. Upon a mesh convergence study (Fig. 13 (b), and (d)), the specimens were discretized by C3D8R element (continuum three dimensional 8 noded reduced integration element) with a size of 0.05 mm for angled specimen and 0.12 mm for FBD specimen, resulting in 173880 and 141636 elements, respectively. The incident bar, transmission bar, and WC platens were also discretized with C3D8R elements with a size of 1.5 mm, 1.5 mm, and 0.5 mm,

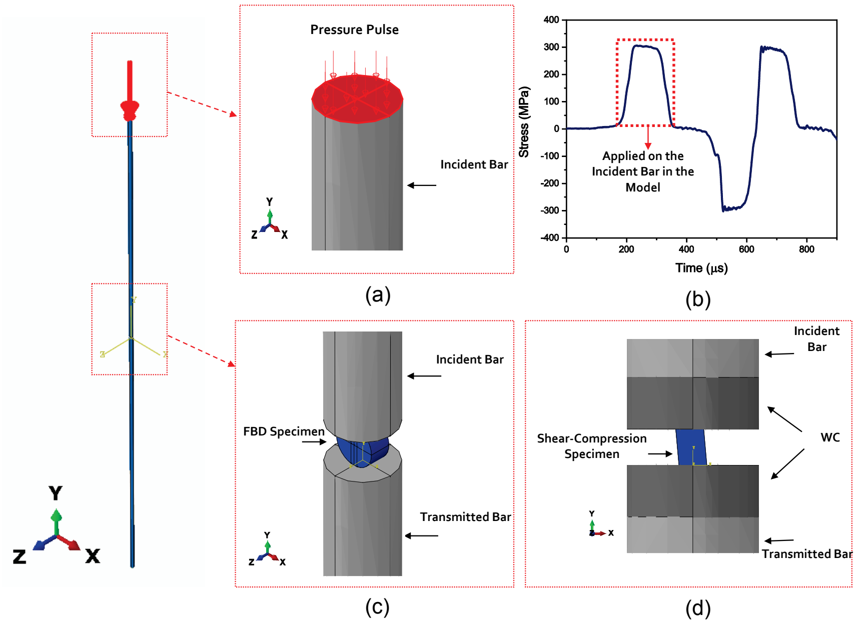

Figure 4: 3D FE model of the SHPB setup used to simulate indirect tension and compression-shear experiments. (a) To simplify the model and decrease the run-time, the incident bar is only modeled between the location of the strain gauge toward the specimen, and the experimentally recorded stress-time pulse in the incident bar is applied as a pressure pulse on the cross-section of the modeled incident bar. (b) The subfigure shows the stress pulse in the incident bar measured through the strain gauge. The area in the red box is used as the input pressure pulse applied on the incident bar as shown in part (a). (c) and (d): The configuration of the indirect tension specimen and compression-shear specimen between the bars.

leading to 33516, 46360 and 6400 elements, respectively. To reduce the run-time, the models were run on Compute Canada Graham cluster. For each simulation, four nodes (i.e., 128 cores) were employed and the corresponding computational times are summarized in Table 3.

4. Results and Discussion

In this section, the results on the dynamic behavior of alumina ceramics under indirect tension and compression-shear loading are outlined for both the experiments and numerical simulations. As outlined in the previous section, the model predictions are validated with the experimental results both qualitatively (e.g., failure initiation and propagation process on the specimen surface) and quantitatively (e.g., stress versus strain and lateral strain versus axial strain responses of the material). Subsequently, the model is exercised to study the effect of the regularization parameters of the JH2-V material model (Section 4.2) and bulking phenomena (Section 4.3). The validated model is employed for studying the effect of shear on failure response of Al_2O_3 ceramics via quantitative analysis of the damage initiation and growth (Section 4.4), and provide guidance for higher-scale applications (e.g., impact) in terms of element size selection (Section 4.5).

4.1 Experimental and Numerical Results for the Mechanical Behavior of Al_2O_3 Ceramics Under Dynamic Indirect Tension and Compression-Shear Loading

The predicted stress-time histories of the alumina ceramics under indirect tension loading at high strain rates (i.e., ranged from 10 to 10^2 s^{-1}) compared with the experimental results are summarized in Fig. 5 (a), (b), and (c). It is observed that, the predicted curves reasonably capture the experimentally measured ones, and the experimental trend of an increase in tensile strength with increasing strain rate is also reflected in the numerically predicted curves. Fig. 5 (d) shows the comparison between the predicted damage initiation and propagation (corresponding to numbered points in the Fig. 5 (b)) and the time-resolved images of crack propagation in the specimen captured through the ultra-high-speed camera. Experiment-wise (see the first row of Fig. 5 (d)), it is observed that damage accumulates at the corners of the specimen in contact with the SHPB bars and starts to propagate along the center of the disk (from point 1 to point 2). At the onset of the peak stress (point 2), an axial primary crack appears at the center of the specimen, and this is followed by the initiation of secondary cracks at the edge of the specimen. Upon peak stress (point 3), multiple primary cracks are observed along the center of the specimen, and secondary circumferential cracks are generated at the edge of the specimen, and this failure process leads to an abrupt decrease in load sustaining capacity and catastrophic failure (point 4). The fracture pattern observed and predicted here has also been observed in previous studies on ceramic materials [78–80], indicating a valid FBD experiment. Numerically (see the second row of Fig. 5 (d)), the experimental failure process is reasonably reproduced. The damage first appears at the two interfaces due to stress concentrations and then starts to accumulate at the central area of the disk. Next, the element deletion process is triggered in the center-line of the disk, and this resembles the formation of the primary crack just before the peak stress. Note that the elements are deleted when the equivalent plastic strain at the integration points exceeds a critical value of 0.2, and this value has been used in previous numerical studies on alumina ceramics [55, 81]. The damage growth at the central area proceeds with the formation of secondary circumferential cracks at the edges which leads to the rapid decrease in the stress; both are consistent with experimental results (the first row of Fig. 5 (d)).

Similarly, the simulated stress-time histories of the alumina ceramics under compression-

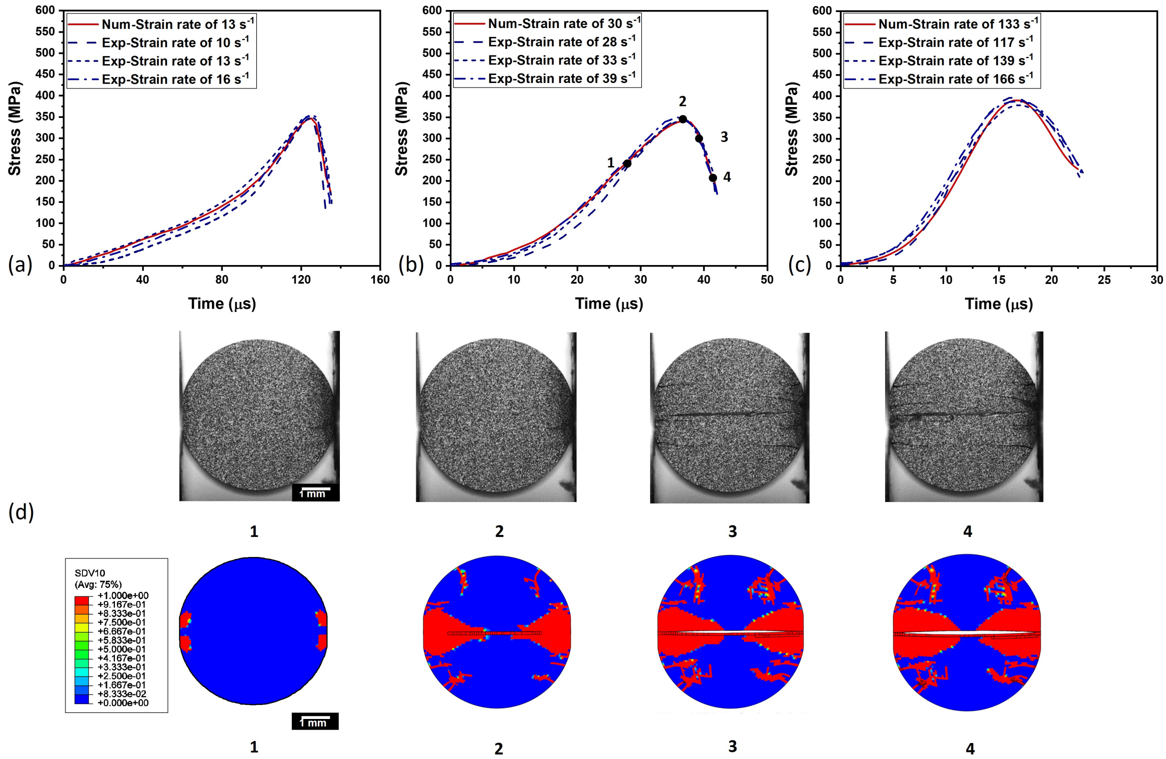

Figure 5: The numerical (Num) and experimental (Exp) stress-time history of ceramic specimens under an indirect tension stress state with corresponding time-resolved images of crack propagation in the specimen captured through the ultra-high-speed camera. The numbered black points on the stress-time plot are selected to make a qualitative comparison between the numerical and experimental results. (a) The experimental and numerical stress-time curves for a strain rate range of 10 to 16 s^{-1}. (b) The experimental (dashed lines) and numerical (solid lines) stress-time curves for a strain rate range of 28 to 39 s^{-1}. (c) The experimental and numerical stress-time curves for a strain rate range of 117 to 166 s^{-1}. (d) The visualization of damage initiation and propagation in indirect tension experiments via ultra-high-speed camera images compared to those of the numerical simulation. Note that, in the numerical legend, SDV10 represents the damage parameter of the JH2-V model (see Eq. (8))

shear stress state at high strain rates (ranged from 10^2 to 10^3 s^{-1}) compared with the experimental results are illustrated in Fig. 6 (a), (b), and (c). In Fig. 6 (a), (b), and (c), the predicted shear strains are also compared with shear strains obtained by the DIC analysis. The experimental curves exhibit a softening regime before the peak stress, which is resulting from the initiation of axial cracks (see the time-resolved image in Fig. 6 (d) corresponding to point 2 in Fig. 6 (c)) and accumulation of damage at the corners. Upon reaching peak stress, the stress-bearing capacity sharply falls due to the abrupt nucleation and growth of multiple axial cracks and their later coalescing. It is observed that, the predicted curves for the ceramic materials reasonably capture the experimental results (Fig. 6 (a), (b), and (c)), which shows the the applicability of the current approach for modeling the alumina ceramics. Showing in the first row of Fig. 6

(d) are time-resolved high-speed images of the structural failure captured experimentally by the ultra-high-speed camera, and those of the FE model corresponding to the black points on Fig. 6 (c) are shown in the second row of Fig. 6 (d)). The first figure shows that damage starts to accumulate on the left side of the specimen (i.e., the contact area with the incident bar) and a longitudinal crack parallel to the angle of the specimen created at the bottom side of the specimen. Prior to failure, more damage is accumulated in the contact area with the incident bar, and the longitudinal crack propagates parallel to the lateral edges (point 2). Upon failure, more cracks nucleate parallel to the lateral edges from both contact areas (point 3). Eventually, the interaction and coalescence of cracks together along the specimen lead to the catastrophic failure of the specimen (point 4).Overall, the rate-dependent behavior of the material (i.e., the increase in tensile and compressive strength with the increase in rate) is also numerically reflected for both FBD and compression-shear loading conditions. The model captures this effect due to the incorporation of the rate-dependent hydrostatic tensile strength of ceramics [27, 48] (see Eq. (6)), and accounting for the effect of inertial confinement [82] implicitly as a bulking-induced increment in pressure (Eq. (11)). The latter is studied in more detail in the following (see Fig. 10).

Lastly, the simulated stress-lateral strain and lateral strain-axial strain history of the specimen under both indirect tension and compression-shear loading (solid lines) are compared with the experimental results represented by dashed lines in Fig. 7. As seen in Fig. 7 (a), in agreement with the linear elastic response in the experiments, the numerical curves also linearly increase up to the peak stress, which confirms the correctness of the developed strain fields in the model. Fig. 7 (b) shows that the collapse in the experimental curves (i.e., after peak stress) follows an upward trend, which indicates the occurrence of an abrupt failure (i.e., outward expansion) caused by unstable structural failure under a tensile-dominated stress state [27, 66]. The numerically predicted lateral strain versus axial strain responses are consistent with the measurements in terms of the Poisson's ratio and the upward trend upon failure. In addition, Fig. 7 (c) shows the experimentally measured stress-axial strain (blue dashed lines) compared with simulation results (a solid red line) under compression-shear loading. It is observed that the stress-axial strain curves are nearly-straight lines and immediately decrease when the curves reach the peak due to catastrophic failure of the specimens, which is also reflected in simulation results. Shown in Fig. 7 (d) is the experimental data (blue dashed lines) of lateral strain-axial strain responses with comparison to numerical results (a solid red line), and the good agreement

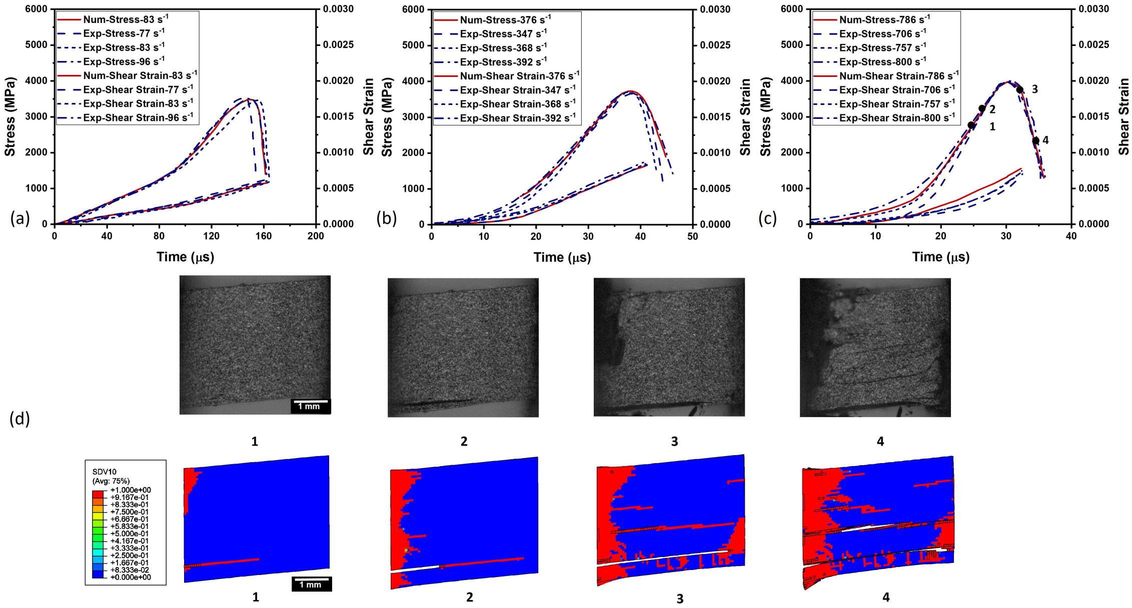

Figure 6: The numerical (Num) and experimental (Exp) stress-time history of ceramic specimens under a compression-shear stress state with corresponding time-resolved images of crack propagation in the specimen captured using the ultra-high-speed camera. The marked points (numbered black points) on the stress-time plot are selected to make qualitative comparisons between the numerical and experimental results. (a) The experimental and numerical stress-time curves for a strain rate range of 77 to 98 s^{-1}. (b) The experimental (dashed lines) and numerical (solid lines) stress-time curves for a strain rate range of 347 to 392 s^{-1}. (c) The experimental and numerical stress-time curves for a strain rate range of 706 to 800 s^{-1}. (d) The visualization of damage initiation and propagation in compression-shear experiments via ultra-high-speed camera images compared to those of the numerical simulation. Note that, in the numerical legend, SDV10 represents the damage parameter of the JH2-V model (see Eq. (8))

indicates that the FE model can well predict the material behavior under combined loading. The presented simulations for FBD and compression-shear loading conditions were also conducted by using the JH2 material model to provide more insights on the improvements in predicted results by the JH2-V model. The reader is referred to Appendix B for more details on comparing the JH2 and JH2-V model.

Overall, the reasonable agreement between the numerical and experimental findings, both quantitatively (e.g., stress-strain and axial strain-lateral strain curves) and qualitatively (e.g., images describing failure process), demonstrates the applicability of the current modelling approach to computationally explore the dynamic behavior of alumina ceramics.

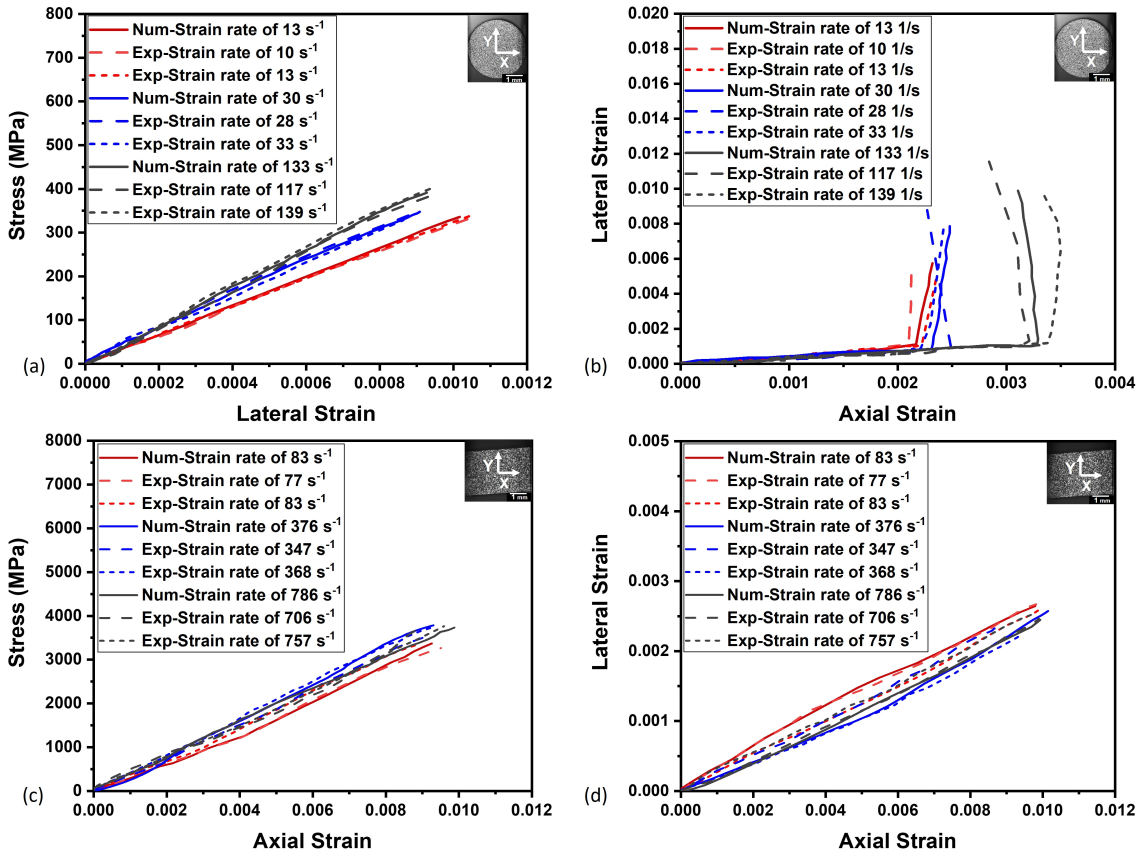

Figure 7: The mechanical response of alumina under indirect tension and compression-shear stress states. (a) Representative numerical (Num) and experimental (Exp) stress-lateral strain responses of the material under indirect tension loading. (b) The numerically predicted lateral strain (Y direction)-axial strain (X direction) history compared to the experimental results measured through DIC analysis. (c) Representative numerical (Num) and experimental (Exp) stress-axial strain responses of the material under compression-shear loading. (d) The numerically predicted lateral strain (Y direction)-axial strain (X direction) history compared to the experimental results measured through DIC analysis.

4.2 Studying the Effect of the JH2-V Model Regularization Parameters on Mechanical Behavior of Al_2O_3 Ceramics under Dynamic Indirect Tension and Compression-Shear Loading

In the JH2-V model, the appropriate selection of the regularization parameters, including η and $\dot{\lambda}_t$, plays an important role on the objectivity of the predicted results in terms of the damage propagation in the material. Fig. 8 shows how the predicted stress and damage propagation evolve in the specimen with the variation of the regularization parameters (i.e., η and $\dot{\lambda}_t$). The final calibrated values for regularization parameters in this study are choosen as η=0.025 MPa·s and $\dot{\lambda}_t$=10000 s^{-1}. First, Fig. 8 (a) and (b) show the predicted stress histories under indirect tension loading by considering a fixed value of $\dot{\lambda}_t$=10000 s^{-1} with different η parameters (Fig. 8

(a)), and a fixed value of η=0.025 MPa·s with different values for $\dot{\lambda}_t$ (Fig. 8 (b)). Corresponding damage profiles are shown in Fig. 8 (c), (d) and (e) at numbered strain levels on Fig. 8 (a) and (b). As seen in Fig. 8 (a), with the increase in the viscous parameter, the load-bearing capacity converges to the response which correlates with the measured one. It is found that when η=0 (i.e., the regularization is suppressed), the predicted peak stress is underestimated and damage accumulates at the corner of the specimen and does not propagate across the specimen (see Fig. 8 (c)), which is not in agreement with the experimental observations (Fig. 5). In Fig. 8 (b), low values of $\dot{\lambda}_t$ results in an underestimation of the material strength as the strain-rate-dependent spall strength of the material is not properly accounted for. Additionally, by choosing higher values for $\dot{\lambda}_t$ (higher values than calibrated data), the predicted stress-time curves converge together, and the corresponding damage profile is shown in Fig. 8 (d). While damage propagates at the central area of the disk, the formation of secondary circumferential cracks is not well predicted when compared to the one predicted by the calibrated $\dot{\lambda}_t$ (see Fig. 8 (e)).

Next, Fig. 9 shows the predicted history of stress and damage propagation pattern in the angled specimen under different variation of regularization parameters. Fig. 9 (a) and (b) show the predicted history of stress under compression-shear loading by considering a fixed value of $\dot{\lambda}_t$=10000 s^{-1} with different η parameters (Fig. 9 (a)), and a fixed value of η=0.025 MPa·s with different values for $\dot{\lambda}_t$. The corresponding damage profiles are shown in Fig. 9 (c), (d) and (e) at numbered strain levels on Fig. 9 (a) and (b). It is found that when η=0 MPa·s where the regularization is suppressed, the predicted peak stress is lower than the measured one and damage accumulates at the center of the specimen (see Fig. 9 (c)). As shown in Fig. 9 (b), the model underestimates the material strength when choosing low values of $\dot{\lambda}_t$, and for higher values of $\dot{\lambda}_t$ the predicted curves converge together. From Fig. 9 (d), it is observed that as damage propagates in the specimen, the formation of the cracks is less accurately predicted in comparison with the predicted one by using the calibrated $\dot{\lambda}_t$ = 10000 s^{-1} (Fig. 9 (e)).

4.3 Studying the Effect of Bulking on Mechanical Behavior of Al_2O_3 Ceramics under Dynamic Indirect Tension and Compression-Shear Loading

In brittle materials, the failure process is dominated by the initiation and growth of cracks, which leads to an incremental increase in the porosity volume of the material [83, 84]. This increase in porosity volume is known as bulking, and bulking plays an important role in failure response of ceramics [83], rocks [85], and concretes [86]. In a study by Simons et al. [57], the

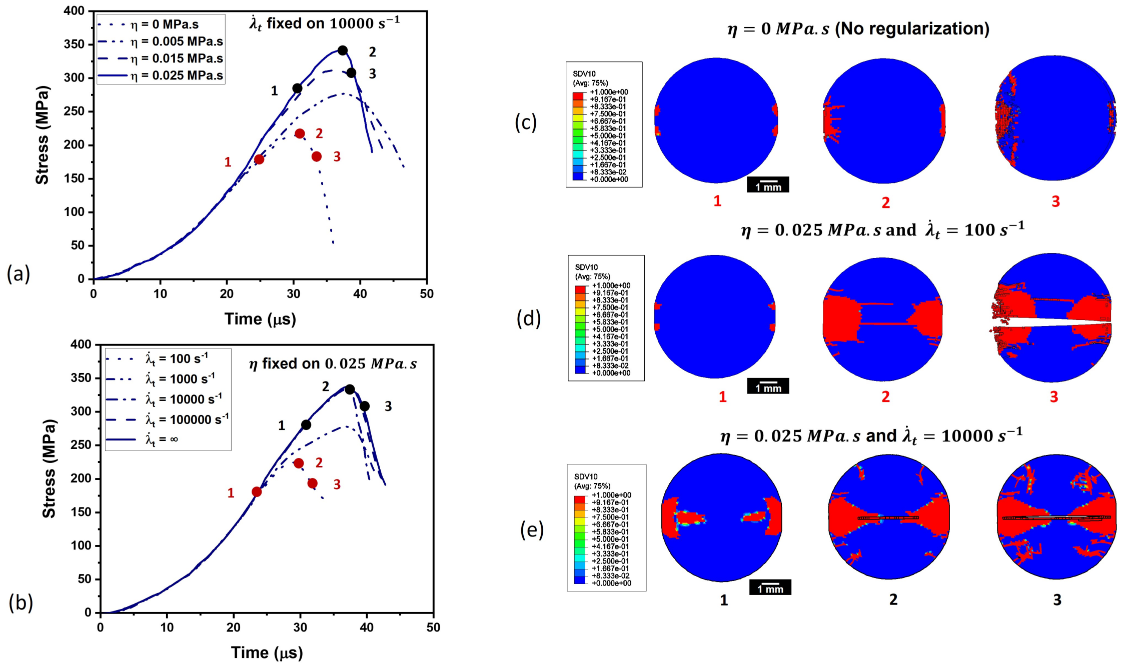

Figure 8: The effect of the JH2-V model regularization parameters: the viscosity parameter (η) and the equivalent plastic strain transition parameter ($\dot{\lambda}_t$), on the predicted indirect tension response. (a) The effect of the η parameter on the predicted stress-time history for indirect tension simulations at a strain rate of 30 s^{-1}. (b) The effect of the $\dot{\lambda}_t$ parameter on the predicted history of stress for indirect tension loading at a strain rate of 30 s^{-1}. As $\dot{\lambda}_t$ exceeds 10000 s^{-1}, the predicted response remains unchanged. (c) Predicted damage pattern when η=0 MPa·s and $\dot{\lambda}_t$=10000 s^{-1} with time corresponding to the red numbered points on the subfigure (a). (d) Predicted damage pattern when η=0.025 MPa·s and $\dot{\lambda}_t$=100 s^{-1} with time corresponding to the red numbered points on the subfigure (b). (e) Predicted damage pattern in indirect tension simulation with time-resolved numbered points on the stress-time responses based on the calibrated constants (black points on the subfigures (a), and (b)). Note that, in the numerical legend, SDV10 represents the damage parameter of the JH2-V model (see Eq. (8))

effect of bulking is considered through the calculation of a volumetric plastic strain component based on the Drucker-Prager plastic potential function. In our developed model in ABAQUS, similar to the original JH2 model [45], we considered the bulking effect as the induction of an increment in pressure when damage evolution is triggered under compression (as detailed in Section 3). Fig. 10 (a) and (c) shows how bulking may affect the predicted peak stress in both indirect tension and compression-shear stress states. Bulking occurs in ceramic materials to accommodate the formation of cracks [83, 84]. As such, when bulking is not considered, the predicted peak stress is slightly underestimated, and this is observed in Fig. 10 (a) and (c). Fig. 10 (b) and (d) draw a comparison between the predicted damage propagation pattern corresponding to the specified numbered points on Fig. 10 (a) and (c) with the bulking effect and the one predicted when the bulking effect is not considered. As shown, the FE model

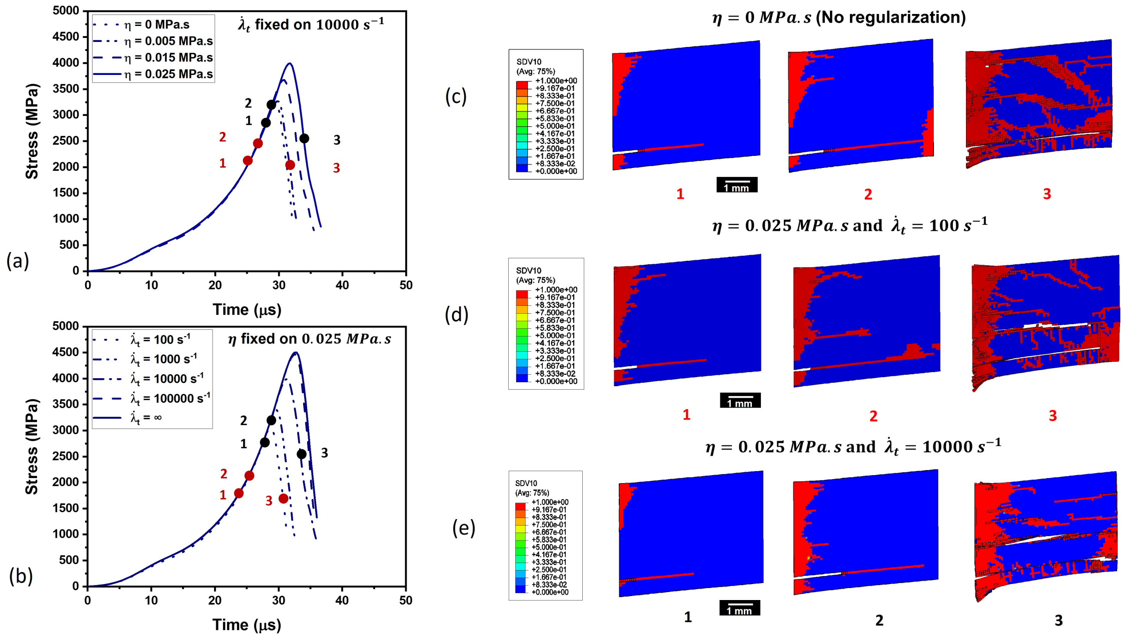

Figure 9: The effect of the JH2-V model regularization parameters: the viscosity parameter (η) and the equivalent plastic strain transition parameter ($\dot{\lambda}_t$) on the predicted compression-shear response.(a) The effect of the η parameter on the predicted stress-time history for compression-shear simulation at a strain rate of 786 s^{-1}. (b) The effect of the $\dot{\lambda}_t$ parameter on the predicted history of stress for the compression-shear response at a strain rate of 786 s^{-1}. As $\dot{\lambda}_t$ exceeds 100000 s^{-1}, the predicted response remains unchanged. (c) Predicted damage pattern with η=0 and $\dot{\lambda}_t$=10000 s^{-1} with time corresponding to the red numbered points on subfigure (a). (d) Predicted damage pattern when η=0.025 MPa·s and $\dot{\lambda}_t$=100 s^{-1} with time corresponding to the red numbered points on the subfigure (b). (e) Predicted damage pattern in compression-shear simulation with time corresponding to the numbered points on the stress-time responses based on the calibrated constants (black points on the subfigures (a), and (b)). Note that, in the numerical legend, SDV10 represents the damage parameter of the JH2-V model (see Eq. (8))

predicts no significant difference in the material response with respect to the bulking effect for the studied conditions. The same result has been also reported for alumina ceramics subject to sphere impact testing [57].

4.4 Application of the Model to Study the Effect of Shear: Compression-Shear Specimen with Different Angles

The presence of shear strain plays an important role during the failure initiation and propagation in brittle materials [19, 87]. Fig. 11 shows the application of the current model for studying the effect of shear strain on the material response and damage growth. The implemented modeling framework has been leveraged to quantitatively analyze the damage initiation and growth in the material to provide insight on the role of shear on the mechanical response. Shown in Fig. 11 (a) are the predicted stress-time curves and the corresponding shear strain-

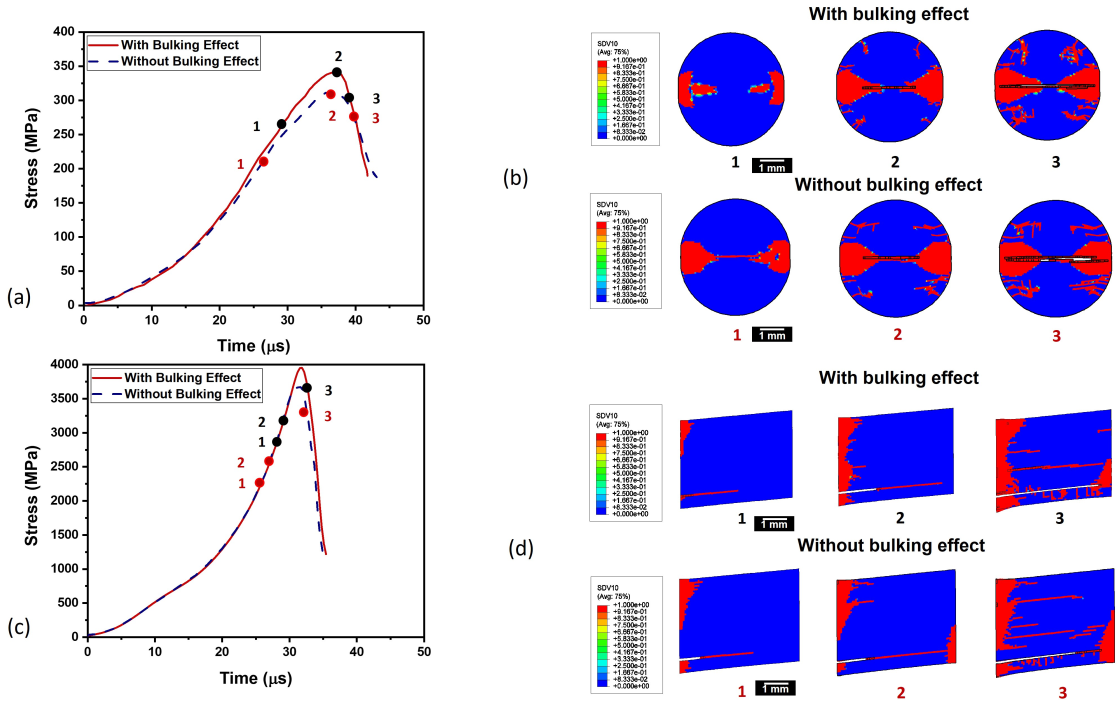

Figure 10: The effect of incorporating bulking in the JH2-V model on the predicted results for the dynamic indirect tension (top b) and compression-shear loadings (bottom d). (a) The effect of bulking on the predicted history of stress-time for the indirect tension test at a strain rate of 30 s^{-1}. (b) The figures show the qualitative history of damage propagation in the material under indirect tension when the bulking effect is and is not considered. The comparison is made at the corresponding numbered points in subfigure (a). The consideration of bulking in the JH2-V model results in the prediction of secondary cracks initiating from the disk circumference. (c) The effect of incorporating bulking on the predicted results for the compression-shear test at a strain rate of 700 s^{-1}. (d) The figures show the qualitative history of damage propagation in the material under compression-shear loading when the bulking effect is and is not considered. The comparison is made at the corresponding numbered points in subfigure (c). Note that, in the numerical legend, SDV10 represents the damage parameter of the JH2-V model (see Eq. (8))

time histories for different angled compression-shear specimens at a fixed strain rate of 780 s^{-1}. It is observed that, by increasing the angle of the specimens, the induced shear strain increases while the peak stress follows a descending trend. To quantify the history of failure initiation and propagation in the material, the damage parameter of the JH2-V model is volumetrically averaged at each increment of the loading history using Python scripting. The average volumetric damage is computed as [88]:

$$D_{avg} = \frac{\sum_i^N D_i V_i}{\sum_i^N V_i} \tag{14}$$

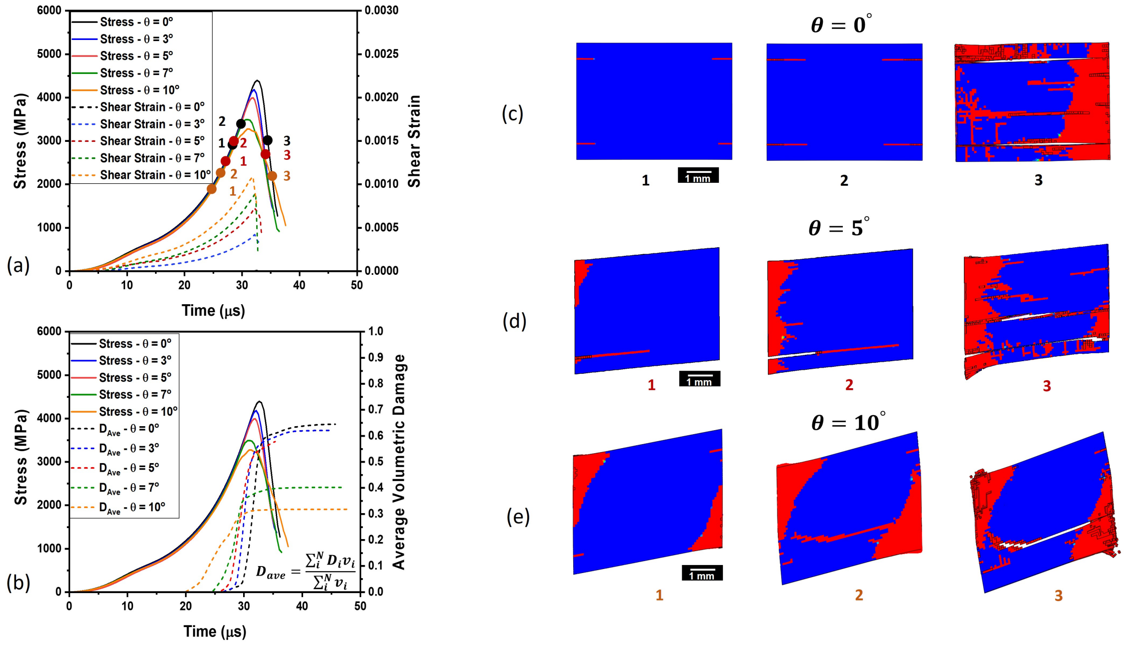

Figure 11: A numerical investigation of the effect of shear on the material behavior by considering different angles ($\theta = 0^{\circ}, 3^{\circ}, 5^{\circ}, 7^{\circ}$ and 10°) in compression-shear testing. (a) Comparing the history of stress and shear strain that shows the shear strain increases with the increase in angle, and this leads to a decrease in the peak stress. (b) Comparing the stress-time history and volumetric average damage growth. With the increase in angle, the damage is initiated earlier in the material. (c), (d), and (e) shows the accumulation of damage in the material at different strains marked on subfigure (a) under different angles of $\theta = 0^{\circ}$ (black point), $\theta = 5^{\circ}$ (blue point) and $\theta = 10^{\circ}$ (red point), respectively. As seen, in all cases, damage accumulates at the corners and then propagates parallel to the specimen angle.

where D_i and V_i are the JH2-V damage parameter and the volume of each integration point of the elements (i.e., the denominator of the Eq. (14) is the total volume of the simulated specimen at each increment of loading), respectively. Fig. 11 (b) shows the predicted stress-time histories and the volumetric average damage-time curves. As seen with the increase in shear strain (i.e., increasing in tilting angles) the damage initiates earlier in the material, and this contributes to a decrease in the peak stress. In addition, the maximum magnitude of damage reduces as a function of peak shear strain. Fig. 11 (c), (d), and (e) show a comparison between the numerically predicted damage propagation patterns in the alumina ceramics with $\theta = 0^{\circ}$, $\theta = 5^{\circ}$ and $\theta = 10^{\circ}$ (for the sake of brevity, the angles of $\theta = 3^{\circ}$ and $\theta = 7^{\circ}$ are not shown) at the strain levels corresponding to the numbered points in black, red, and orange, respectively, in Fig. 11 (a). As shown, by increasing the angle of the specimen and increasing the effect of shear deformation, damage tends to localize at the corners, and less damage propagation, and branching are observed.

Fig. 12 (a) shows the pattern of shear strain in the compression-shear model with different angles to provide a better understanding of how the shear strain is spatially affected. As seen, with the increase in the angle of the compression-shear model, the shear strain mainly increases in the central area and the shear strain at the corners is less affected. Note that Fig. 12 (a) corresponds to the time of 20 μs in Fig. 11 (a), when no damage is developed in the models to affect the strain distribution pattern. To confirm this observation, a p-q diagram is plotted at different locations (labeled as P1, P2, P3, P4, P5, P6, and P7 in Fig. 12 (a)) up to failure on the compression-shear model with different angles. The slope of the p-q curve reflects the inverse of the stress triaxiality parameter; the more the stress triaxiality, the less the effect of shear [89]. Accordingly, the p-q curve with a higher slope represents the presence of more shear. As seen in Fig. 12 (b), with the increase in the angle of the model, the level of shear increases minimally at the corners represented by P1 and P2 points on Fig. 12 (a), while the maximum increase occurs at the center represented by P5 (i.e., the highest increase in the slope of the p-q curve). This implies that higher-angled specimens induce more shear deformation in the material locally with a predominant increase in the central area.

4.5 Application of the Model for Guidance in Higher Scale Modeling

In real applications such as protection systems against ballistic impact, ceramics experience mixed-mode stress states that evolve spatially and temporally [90]. For the efficient use of FE modelling of ceramics at structural scales, minimizing the run-time by selecting appropriate element sizes is of great importance [76]. In this section, the current modelling framework is used to provide some guidance on the element size selection based on the stress-state-dependent mesh sensitivity of the stress-time results. Fig. 13 shows the predicted time history of stress in the material subject to dynamic compression-shear loading with different angles, namely $\theta = 0^{\circ}$, $\theta = 5^{\circ}$, and $\theta = 10^{\circ}$, as well as the FBD specimen under indirect tension loading when different element sizes are selected. As seen in Fig. 13 (a), (b), and (c), the stress state varies from uniaxial compression to shear-dominated with an increase in angle from $\theta = 0^{\circ}$ to $\theta = 10^{\circ}$. It is observed that, for all the stress states, with the decrease in the element size from 0.14 mm (7000 elements) to 0.03 mm (800000 elements), the slope of the curve remains constant while the peak stress follows a descending trend towards convergence. In addition, Fig. 13 (a), (b), and (c) shows that the mesh sensitivity is affected by the stress states. Specifically, the maximum sensitivity is observed under uniaxial compression with a variation of 27% in the peak stress when going from an element size of 0.03 mm to 0.14 mm, and the minimum sensitivity

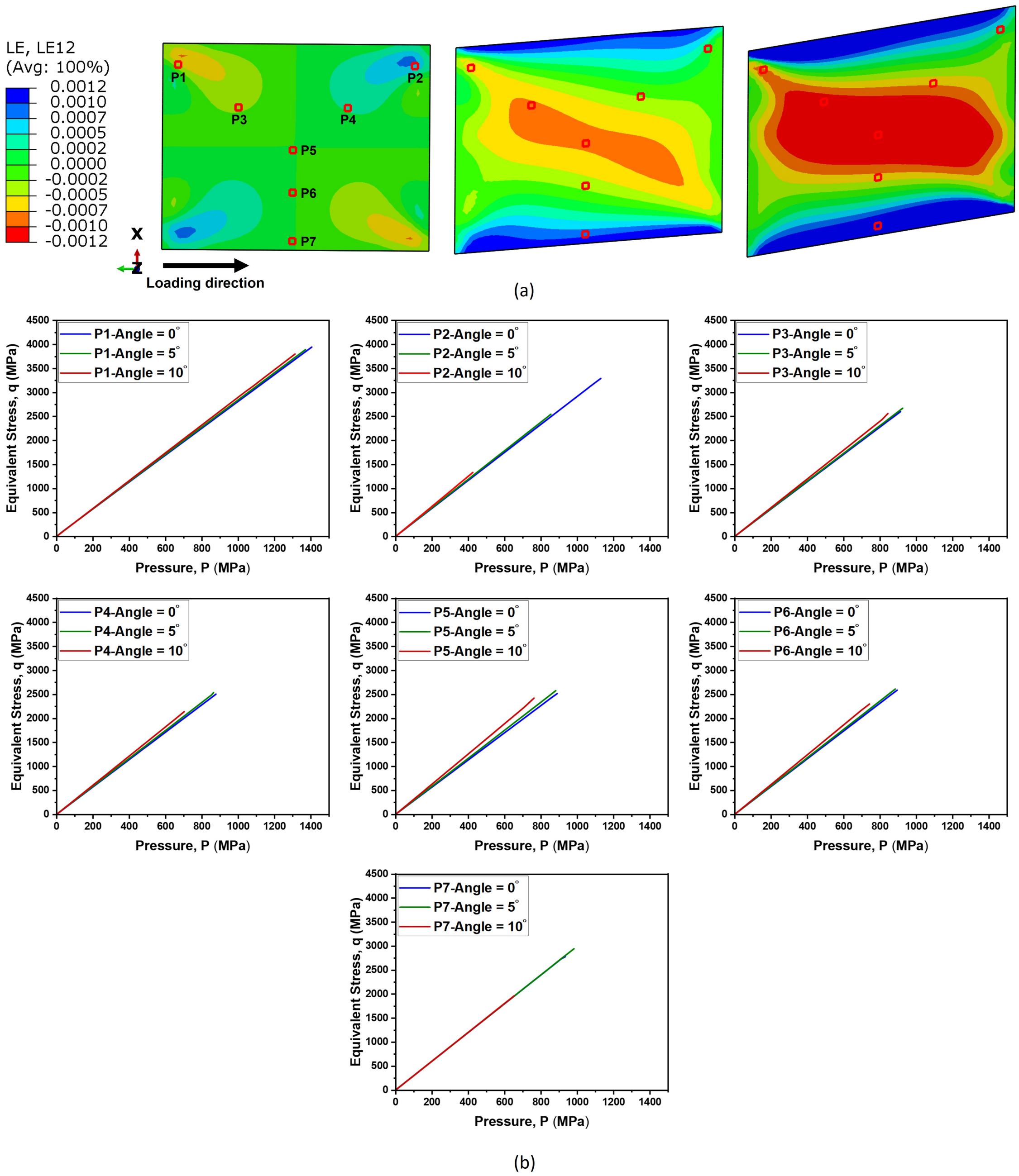

Figure 12: A numerical investigation of the effect of the angle of the compression-shear specimen on the spatial distribution pattern of shear strain and its quantity. (a) The contour of shear strain distribution in the compression-shear model with different angles ($\theta = 0^{\circ}$, 5°, and 10°) at a time of 20 μs (see Fig. 11 (a)). (b) The p-q diagram plotted at the labeled locations on the sub-figure (a) up to failure for the compression-shear model with different angles. Note that, in the numerical legend, LE represents the shear strain in the X-Y plane.

is obtained at the angle of $\theta = 10^{\circ}$ as the shear-dominated stress state with a variation of 14.5% in the peak stress across the same range of element sizes. Also note that the variation follows a negative correlation with increasing angles (i.e., increasing in shear dominance leads to a decrease in mesh sensitivity). Fig. 13 (d) shows that the predicted results are least affected by the element size for a tension-dominated stress state. As a result, the model predicts the failure response is insensitive to element size under tensile loading, and the greatest mesh dependency is introduced into the predicted failure response when a compression-dominated stress state is induced in the material. This pattern of mesh sensitivity is attributable to how the regularization method is applied in the JH2-V model, which is also related to why mesh sensitivity is mitigated in this model when compared to the JH2 model (see Appendix B). The tensile strength of the material is increased the most (i.e., maximal regularization) by the proposed rate dependency model – which is also involved in the viscosity regularization approach (see Eq. (6)) – in the JH2-V model, while the minimal increase (i.e., minimal regularization) is applied on the strength under high pressure. As such, under tensile-dominated stress states, the regularization method is the most influenced, and with the increase in the presence of compression, the effect of regularization decreases. Accordingly, the minimum mesh sensitivity ($\sim$ 1%) is observed for FBD simulation results, and the maximum mesh sensitivity (27%) is observed for uniaxial compression simulation results (i.e., compression-shear sample with an angle of 0°).

Table 3 summarizes different element sizes and the corresponding run-time used for the simulation of compression-shear specimen with an angle of $\theta = 5^{\circ}$ and the FBD specimen. For the compression specimen, the peak stress varies 27% from the coarse mesh to the fine mesh which is notably lower than previous studies with the JH2 model [76, 91, 92]: this is attributable to the mesh sensitivity mitigation in the JH2-V model. As the mesh size decreases to 0.05 mm and below, the peak stress remains almost unaltered while the run-time increases by $\sim$ 125% from 24 to 54 hours. For the FBD specimen, the peak stress remains almost the same with a variation of $\sim$ 1% from coarse mesh to fine mesh, representing less mesh sensitivity when compared to compression-shear loading. From Table 3, as the mesh size decreases to 0.12 mm and below the run-time increases by $\sim$ 476% from 1.3 to 7.5 hours.

As such, to balance between the computational cost and accuracy, an element size of 0.05 mm and 0.12 mm has been chosen for further simulations of compression-shear and tension loading in this study, respectively. Based on this outcome, for the application of the JH2-V model for ceramics at higher scale modellings, a fine mesh size ($\sim$ 0.05 mm) is recommended for compression-dominated areas while a coarser mesh size may be applied to shear and tension-dominated areas to balance the computational cost and accuracy. This outcome helps avoiding the unnecessary use of fine mesh at the relevant parts of the model to be identified based on the dominant stress state to obtain converged results.

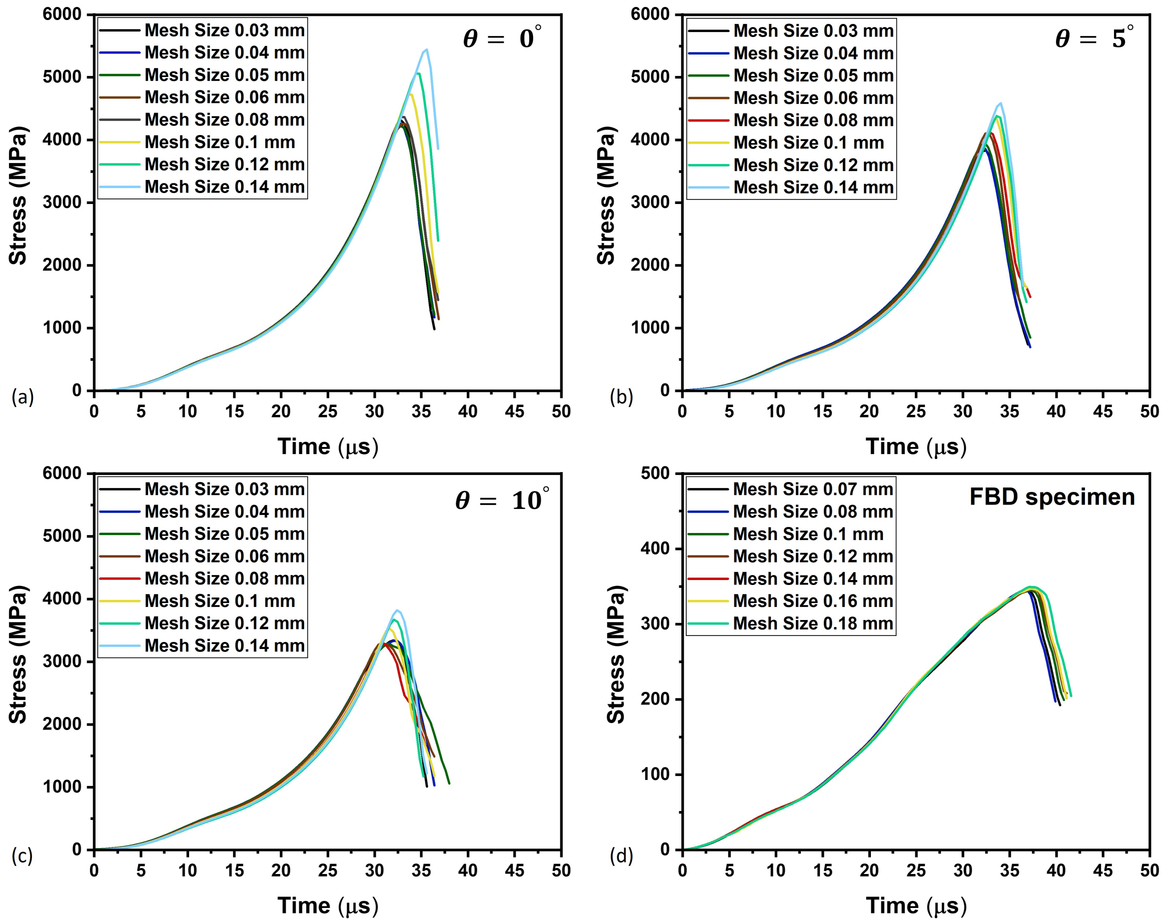

Figure 13: The effect of element size on the predicted stress-time history for compression-shear specimens with different angles ($\theta = 0^{\circ}$, $\theta = 5^{\circ}$, and $\theta = 10^{\circ}$) and FBD specimen. (a) The predicted history of stress-time for an angle of $\theta = 0^{\circ}$. (b) The predicted stress-time curves for an angle of $\theta = 5^{\circ}$. (c) The stress-time response for an angle of $\theta = 10^{\circ}$. (d) The stress-time response for the FBD specimen.

So far, limited efforts have been made to address the effect of the shear strain under compressive loading in ceramics, where the previous studies were mainly focused on rocks [40, 42, 43] and glasses [93, 94] subjected to a combined compression-shear loading by using experimental testing. Additionally, this study provided a foundation to quantitatively analyze the damage accumulation in ceramic materials through numerical modeling, which has been mostly studied qualitatively by presenting time-resolved experimental images [19, 66] or numerical contours [6, 71] in the literature. Finally, the implemented JH2-V model in this study could be improved to better account for the stress-state-dependent failure of ceramics by incorporating Lode angle and stress triaxiality parameters [95, 96], and the asymmetry of damage growth under tension and compression by defining separate corresponding damage evolution laws [95, 96]. This facilitates the efficient design of high-performing ceramics that have tailored mechanical properties [97–100].

Table 3: Mesh sensitivity analysis for the compression-shear specimen with an angle of 5° and FBD specimen: A summary of different mesh sizes, the associated run-time, and the simulated peak stress.

Compression-shear specimen

Mesh size	Number of elements	Run-time (hours)	Peak stress (MPa)
0.03	810810	54	3835
0.04	341088	36	3867
0.05	173880	24	3940
0.06	100890	16	4107
0.08	43384	11	4130
0.1	21735	8	4348
0.12	12673	6	4386
0.14	7600	4.5	4588

Indirect tension (FBD) specimen

Mesh size	Number of elements	Run-time (hours)	Peak stress (MPa)
0.07	687420	7.5	347
0.08	470000	4.5	348
0.1	239360	2.5	348
0.12	141636	1.3	348
0.14	90016	0.86	349
0.16	57500	0.75	350
0.18	39248	0.68	352

5. Conclusion

This study explored the behavior of CeramTec ALOTEC 98% alumina (Al_2O_3) ceramic under dynamic indirect tension and compression-shear loading via FE modeling with experimental validation. Experimentally, angled specimens were used to generate a compression-shear stress state in the material, and a tension-dominated stress state was induced through the FBD specimens. Numerically, the JH2-V model was implemented in ABAQUS software by using a VUMAT subroutine. The FE model was validated both quantitatively (i.e., stress-strain and axial strain-lateral strain responses) and qualitatively (i.e., the manifestation of damage initiation and accumulation), and a reasonable agreement was observed with the experiments. Overall, the results generated in this study will provide insights on:

1. For both indirect tension and compression-shear loading, the model showed that the peak stress is slightly underestimated when the effect of bulking is not considered, and the damage patterns remained almost independent of the bulking effect. This provides a better understanding of how the dominant stress state affects the volume increase of the material due to the accumulation of damage.

2. The pattern of damage propagation under the indirect tension is highly affected by the regularization parameters of the JH2-V model when compared to that of the compression-shear stress state. Quantitatively, for both stress states, the predicted stress-time curves converged with increasing the regularization parameters.

3. A new quantified damage analysis was proposed to provided a better understanding of the relationships between damage accumulation and shear deformation in ceramics, which has been qualitatively addressed in previous studies by presenting time-resolved experimental images. It was found that when more shear strain (i.e., compression-shear specimen with higher angles) is induced in the material the damage accumulation triggered earlier which led to a decrease in the peak stress. In addition, the magnitude of damage decreased with the increase in shear.

4. The effect of element size was studied under different stress states, including uniaxial compression, compression-shear, and tension-dominated stress state. Accordingly, to balance the computational cost and accuracy, for compression-dominated areas a fine mesh size (~ 0.05 mm) is recommended, while a coarser mesh size may be applied to shear and tension-dominated areas of the model when applied to higher-scale applications of ceramics such as impact.

Altogether, the outcome of this study provided a better understanding of the effect of stress state and rate of loading on the failure response of alumina ceramics and the applicability of the current modeling approach to computationally explore the material behavior.

6. Acknowledgment

This work is supported by Defense Research and Development Canada (DRDC), General Dynamics Land Systems – Canada, and NP Aerospace through NSERC Alliance project

ALLRP 560447-2020. The views and conclusions contained in this document are those of the authors and should not be interpreted as representing the official policies, either expressed or implied, of General Dynamics, NP Aerospace, DRDC or the Government of Canada. The Government of Canada is authorized to reproduce and distribute reprints for Government purposes notwithstanding any copyright notation herein. Additionally, this research was enabled in part by support provided by Compute Ontario (www.computeontario.ca/) and Compute Canada (www.computecanada.ca) via the Graham cluster.

Appendix A. The Implementation of the JH2-V Model

In the following, the procedure for the implementation of the JH2-V model by using a VUMAT subroutine is summarized. Fig. A.14 shows the flowchart for the implementation of the material model.

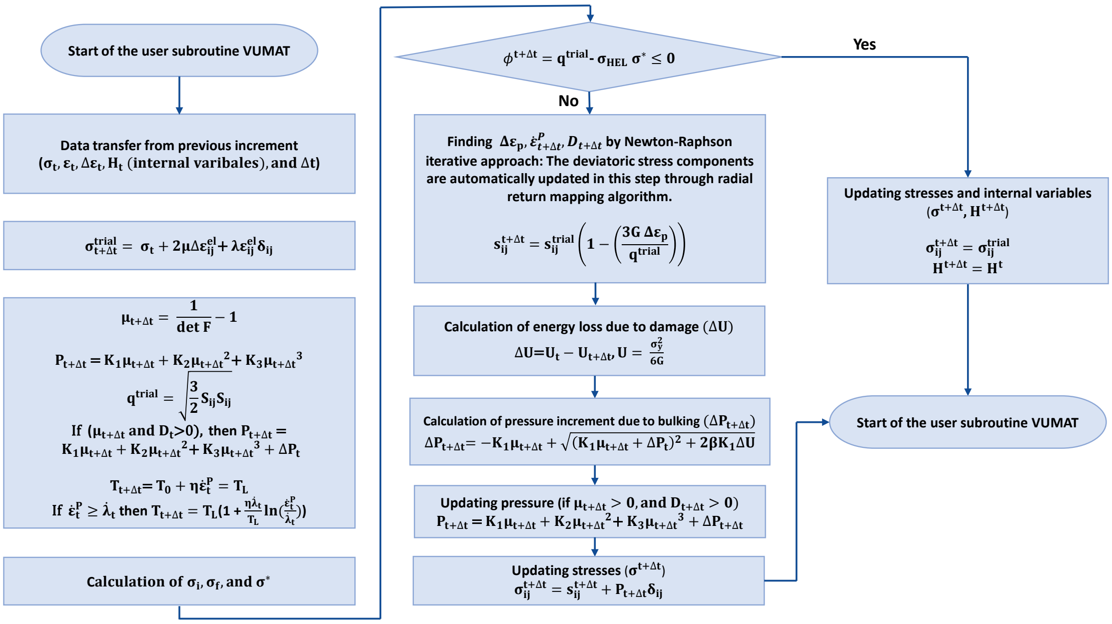

Figure A.14: Flowchart for the implementation of the JH2-V material model via VUMAT subroutine in ABAQUS FE solver.

Upon failure (i.e., $\phi^{t+\Delta t} > 0$), to update the stress components and internal variables (e.g., equivalent plastic strain (ϵ_p), damage parameter (D), and the increment of pressure due to bulking ΔP) ,the admissible equivalent plastic strain ($\Delta\epsilon_p$) is calculated based on an Euler backward formulation [56] through an iterative Newton-Raphson scheme. First, the following variables ($\Delta\epsilon_p{}^{(0)}$, and $\dot{\epsilon}^{(0)}_{p,t+\Delta t}$) are calculated by setting the initial guess (i.e., i = 0) for $\Delta\epsilon_p$ to zero:

$$\Delta\epsilon_p{}^{(0)} = 0 \tag{A.1}$$

$$\dot{\epsilon}^{(0)}_{p,t+\Delta t} = \frac{\Delta\epsilon_p^{(0)}}{\Delta t} \tag{A.2}$$

$$\phi^0 = \phi(\sigma^{(0)}_{t+\Delta t}, \epsilon_{p,t} + \Delta\epsilon_p{}^{(0)}, \dot{\epsilon}^{(0)}_{p,t+\Delta t}) \tag{A.3}$$

Next, the iterative Newton-Raphson method is implemented to find $\Delta\epsilon_p$ based on the following loop until convergence is reached (i.e., $|\phi^{(i+1)}|\leq \delta$, and δ is a threshold value is set to 10^{-8} in this study):

1. $H^i = [{D_e}^{-1} + {\Delta\epsilon_p}^{(i)} \frac{\partial^2\phi}{\partial\sigma^2}]^{-1}$
2. $\beta = (\frac{\partial\phi}{\partial\sigma})^T H[\frac{\partial\phi}{\partial\sigma} + {\Delta\epsilon_p}^{i} \frac{\partial^2\phi}{\partial\sigma\partial\epsilon_p} + \frac{{\Delta\epsilon_p}^{(i)}}{\Delta t} \frac{\partial^2\phi}{\partial\sigma\partial\dot{\epsilon}_p}] - \frac{\partial\phi}{\partial\epsilon_p} - \frac{1}{\Delta t}\frac{\partial\phi}{\partial\dot{\epsilon}_p}$
3. $\Delta\epsilon_p^{(i+1)} = \Delta\epsilon_p^{(i)} + \frac{\phi^{(i)}}{\beta}$
4. $\sigma_{t+\Delta t}^{(i+1)} = \sigma_t + D_e[\Delta\epsilon - \Delta\epsilon_p^{(i+1)} \frac{\partial\phi}{\partial\sigma}]$
5. $\phi^{(i+1)} = \phi(\sigma_{t+\Delta t}^{(i+1)}, \epsilon_{p,t} + \Delta\epsilon_p^{(i+1)}, \dot{\epsilon}_{p,t+\Delta t}^{(i+1)})$
6. if $|\phi^{(i+1)}| > \delta$ goto 1

   else leave the loop and go to the calculation of ΔU (see Fig. A.14)

where D_e is the elastic stiffness tensor. Note that the equations in steps 1 to 6 are taken from Wang et al. [56]. In this study, $(\frac{\partial\phi}{\partial\sigma}^T)H(\frac{\partial\phi}{\partial\sigma})$, $\frac{\partial\phi}{\partial\sigma\partial\epsilon_p}$, $\frac{\partial^2\phi}{\partial\sigma\partial\dot{\epsilon}_p}$, $\frac{\partial\phi}{\partial\epsilon_p}$, and $\frac{\partial\phi}{\partial\dot{\epsilon}_p}$ are derived as Eq. (A.4), Eq. (A.5), Eq. (A.6), Eq. (A.7), and Eq. (A.12), respectively.

$$(\frac{\partial\phi}{\partial\sigma}^T)H(\frac{\partial\phi}{\partial\sigma}) = G \tag{A.4}$$

$$\frac{\partial^2\phi}{\partial\sigma\partial\epsilon_p} = 0 \tag{A.5}$$

$$\frac{\partial^2\phi}{\partial\sigma\partial\dot{\epsilon}_p} = 0 \tag{A.6}$$

$$\frac{\partial\phi}{\partial\epsilon_p} = \frac{(\sigma_i - \sigma_f)\sigma_{HEL}}{\epsilon_p^f} \tag{A.7}$$

$$\sigma_i = A(\frac{T(\dot{\epsilon}_p)}{P_{HEL}} + \frac{P}{P_{HEL}})^n = AQ^n \tag{A.8}$$

Note that the logarithmic formulation for the hydrostatic tensile strength (Eq. (6)) must be used when $\dot{\epsilon}_p \geq \dot{\lambda}_t$.

$$Q = \begin{cases} \frac{T_0+\eta\dot{\epsilon}_p+P}{P_{HEL}}, & \text{for } \dot{\epsilon}_p < \dot{\lambda}_t \\ \frac{T_t(1+\frac{\eta\dot{\lambda}_t}{T_t}(\ln\dot{\epsilon}_p/\dot{\lambda}_t))+P}{P_{HEL}}, & else \end{cases} \tag{A.9}$$

$$\frac{\partial Q}{\partial \dot{\epsilon}_p} = \begin{cases} \frac{\eta}{P_{HEl}}, & \text{for } \dot{\epsilon}_p < \dot{\lambda}_t \\ \frac{\eta\dot{\lambda}_t}{P_{HEL}\dot{\epsilon}_p}, & else \end{cases} \tag{A.10}$$

$$\sigma_f = B(\frac{P}{P_{HEL}})^m = B(P^*)^m \tag{A.11}$$

$$\frac{\partial \phi}{\partial \dot{\epsilon}_p} = -\sigma_{HEL} A Q^{n-1} \frac{\partial Q}{\partial \dot{\epsilon}_p}[1-D] \tag{A.12}$$

$$D = \sum \frac{\Delta\epsilon_p^{eff}}{\epsilon_p^f} \tag{A.13}$$

$$\epsilon_p^f = \begin{cases} \epsilon_p^{min}, & p < p_t \\ \frac{p(\sigma)-p(t)}{p(c)-p(t)}(\epsilon_p^{max} - \epsilon_p^{min}) + \epsilon_p^{min}, & p_t < p < p_c,\ and \\ \epsilon_p^{max}, & p_c < p \end{cases} \tag{A.14}$$

Appendix B. Comparison between the JH2 Model and the JH2-V Model

In this study, the simulations for both the FBD and compression-shear conditions represented in Fig. 5 and Fig. 6, respectively, were conducted with the JH2 model available in ABAQUS software as a built-in material model. The constants used for the JH2 model are exactly the same as the ones used for the JH2-V model represented in Table 2. The JH2 model constants for fracture strain, including d_1, and d_2 were taken from the literature [6] for alumina ceramics. Fig. B.15 compares the predicted results from the JH2 and JH2-V models in terms of stress-time histories and damage patterns for a coarse to a fine mesh size (see Table 3 for more details). As seen in Fig. B.15 (a), for the FBD loading condition where the stress state is tensile dominated, the predicted curves by the JH2 model represent dependency on the element size, while the ones by the JH2-V model are mesh insensitive. Particularly, under a tensile-dominated stress state, the damage pattern is significantly affected by the mesh size in the JH2 model when compared to the JH2-V model. As shown in Fig. B.15 (c), for a coarse mesh size, the JH2 model damage pattern is localized in the contact regions and no propagation is caught in the central area, while that of the JH2-V model reasonably captures the experimentally observed damage propagation pattern, and this is attributable to the viscosity regularization method incorporated into the JH2-V model. As shown in Fig. B.15 (b), the JH2 model predicts more mesh-sensitive stress-time responses under compression-shear stress states when compared to the JH2-V model; The peak stress varies by 41% and 27% predicted by the JH2 and JH2-V model, respectively, from the coarse to the fine mesh size. Similar to the FBD loading conditions, when a coarse mesh is applied to the model, the JH2 model fails to capture the major features of the damage pattern (e.g., the growth of primary axial cracks) in compression-shear stress state (see Fig. B.15 (d)), while the predicted damage pattern by the JH2-V model is in a better agreement with the experiments. Likewise, when the model is discretized by a fine mesh, the JH2 damage pattern and deletion of elements tend to localize at the corners when compared to that of the JH2-V model where the damage growth pattern is more consistent with the experiments (e.g., the growth of an axial crack at the bottom side of the sample). Overall, the JH2-V model improves on the JH2 model in terms of the dependency of qualitative and quantitative results on the mesh and stress-state-dependent damage growth due to the viscosity regularization that leads to a rate-dependent yield surface.

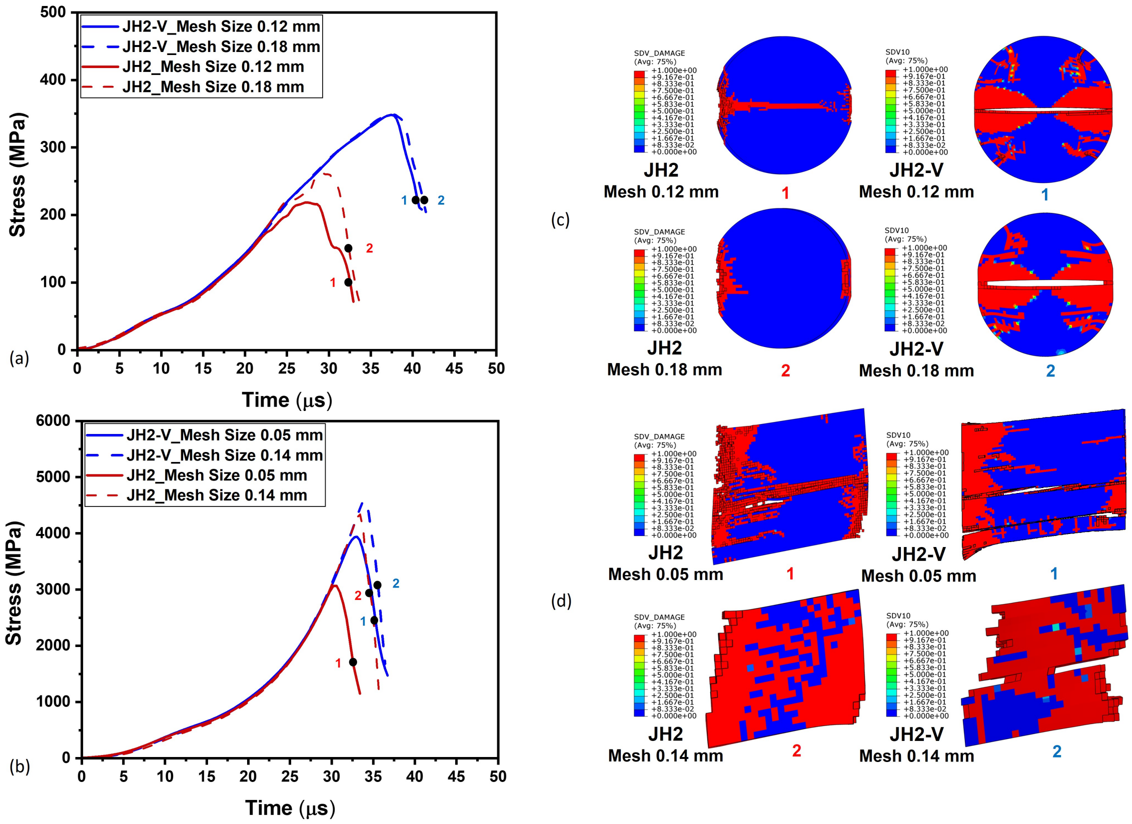

Figure B.15: Comparison of the JH2 and JH2-V models for predicting the response of the alumina ceramics under FBD and compression-shear loading conditions. (a) The predicted stress-time histories of the simulated FBD sample discretized with coarse (0.18 mm) and fine (0.12 mm) mesh size subjected to a strain rate of 30 s^{-1}. (b) Comparing the predicted pattern of damage growth by the JH2 and JH2-V models in the FBD sample. (c) The predicted stress-time histories of the simulated compression-shear sample discretized with coarse (0.14 mm) and fine (0.05 mm) mesh size subjected to a strain rate of 786 s^{-1}. (d) Comparing the predicted pattern of damage growth by the JH2 and JH2-V models in the compression-shear sample. Note that, in the numerical legend, SDV_DAMAGE and SDV10 represent the damage parameter of the JH2 and JH2-V models, respectively.

References

[1] M. R. I. Islam, J. Zheng, and R. C. Batra, "Ballistic performance of ceramic and ceramic-metal composite plates with JH1, JH2 and JHB material models," *International Journal of Impact Engineering*, vol. 137, p. 103 469, 2020, ISSN: 0734-743X.

[2] E. Medvedovski, "Ballistic performance of armour ceramics: Influence of design and structure. part 1," *Ceramics International*, vol. 36, no. 7, pp. 2103–2115, 2010.

[3] R. Savino, L. Criscuolo, G. D. Di Martino, and S. Mungiguerra, "Aero-thermo-chemical characterization of ultra-high-temperature ceramics for aerospace applications," *Journal of the European Ceramic Society*, vol. 38, no. 8, pp. 2937–2953, 2018.

[4] N. P. Padture, "Advanced structural ceramics in aerospace propulsion," *Nature materials*, vol. 15, no. 8, pp. 804–809, 2016.

[5] Z. Zaiemyekeh, G. Liaghat, and M. K. Khan, "Effect of Al2O3 nanoparticles on the mechanical behaviour of aluminium-based metal matrix composite synthesized via powder metallurgy," *Proceedings of the Institution of Mechanical Engineers, Part L: Journal of Materials: Design and Applications*, vol. 235, no. 10, pp. 2340–2355, 2021.

[6] Z. Wang and P. Li, "Dynamic failure and fracture mechanism in alumina ceramics: Experimental observations and finite element modelling," *Ceramics International*, vol. 41, no. 10, pp. 12 763–12 772, 2015.

[7] J. Delage, E. Saiz, and N. Al Nasiri, "Fracture behaviour of Sic/Sic ceramic matrix composite at room temperature," *Journal of the European Ceramic Society*, 2022.

[8] M. Devries *et al.*, "Quasi-static and dynamic response of 3D-printed alumina," *Journal of the European Ceramic Society*, vol. 38, no. 9, pp. 3305–3316, 2018, ISSN: 0955-2219.

[9] J. Pittari, G. Subhash, J. Zheng, V. Halls, and P. Jannotti, "The rate-dependent fracture toughness of silicon carbide-and boron carbide-based ceramics," *Journal of the European Ceramic Society*, vol. 35, no. 16, pp. 4411–4422, 2015.

[10] S. Yang, S. Yang, Y. Zhu, L. Fan, and M. Zhang, "Flash sintering of dense alumina ceramic discs with high hardness," *Journal of the European Ceramic Society*, vol. 42, no. 1, pp. 202–206, 2022.

[11] T. J. Holmquist, D. W. Templeton, and K. D. Bishnoi, "Constitutive modeling of aluminum nitride for large strain, high-strain rate, and high-pressure applications," *International Journal of Impact Engineering*, vol. 25, no. 3, pp. 211–231, 2001.

[12] S. K. Lahiri, A. Shaw, and L. Ramachandra, "On performance of different material models in predicting response of ceramics under high velocity impact," *International Journal of Solids and Structures*, vol. 176-177, pp. 96–107, 2019.

[13] E. Strassburger, "Visualization of impact damage in ceramics using the edge-on impact technique," *International Journal of Applied Ceramic Technology*, vol. 1, no. 3, pp. 235–242, 2004.

[14] A. Bhattacharjee, A. Bhaduri, R. C. Hurley, and L. Graham-Brady, "Failure modeling and sensitivity analysis of ceramics under impact," *Journal of Applied Mechanics*, vol. 88, no. 5, p. 051 007, 2021.

[15] J. Zinszner, B. Erzar, P. Forquin, and E. Buzaud, "Dynamic fragmentation of an alumina ceramic subjected to shockless spalling: An experimental and numerical study," *Journal of the Mechanics and Physics of Solids*, vol. 85, pp. 112–127, 2015.

[16] B. M. Koch, C. Lo, H. Li, T. Sano, J. Ligda, and J. D. Hogan, "Dynamic mechanical response of damaged alumina AD995," *Journal of the European Ceramic Society*, vol. 41, no. 3, pp. 2034–2048, 2021.

[17] C. Lo, T. Sano, and J. D. Hogan, "Deformation mechanisms and evolution of mechanical properties in damaged advanced ceramics," *Journal of the European Ceramic Society*, vol. 40, no. 8, pp. 3129–3139, 2020.

[18] T. Sano *et al.*, "Correlation of microstructure to mechanical properties in two grades of alumina," in *TMS Annual Meeting & Exhibition*, Springer, 2018, pp. 75–81.

[19] B. M. Koch, C. Lo, H. Li, T. Sano, J. Ligda, and J. D. Hogan, "Two-dimensional dynamic damage accumulation in engineered brittle materials," *Engineering Fracture Mechanics*, vol. 244, p. 107 539, 2021.

[20] R. Zhang, B. Han, and T. J. Lu, "Confinement effects on compressive and ballistic performance of ceramics: A review," *International Materials Reviews*, vol. 66, no. 5, pp. 287–312, 2021.

[21] T. Sathish, S. Arunkumar, R. Saravanan, and V. Dhinakaran, "Experimental investigation on material characterization of zirconia reinforced alumina ceramic composites via powder forming process," in *AIP Conference Proceedings*, AIP Publishing LLC, vol. 2283, 2020, p. 020 124.

[22] J. Gong, B. Deng, and D. Jiang, "The efficiency of normal distribution in statistical characterization of the experimentally measured strength for ceramics," *Journal of Materials Engineering and Performance*, vol. 30, no. 1, pp. 42–55, 2021.

[23] G. Subhash, A. Awasthi, and D. Ghosh, *Dynamic Response of Advanced Ceramics*. John Wiley & Sons, 2021.

[24] M. Fejdyś, K. Kośla, A. Kucharska-Jastrzabek, and M. Łandwijt, "Influence of ceramic properties on the ballistic performance of the hybrid ceramic–multi-layered UHMWPE composite armour," *Journal of the Australian Ceramic Society*, vol. 57, no. 1, pp. 149–161, 2021.

[25] H. Mei, Y. Tan, W. Huang, P. Chang, Y. Fan, and L. Cheng, "Structure design influencing the mechanical performance of 3D printing porous ceramics," *Ceramics International*, vol. 47, no. 6, pp. 8389–8397, 2021.

[26] C. Lo, T. Sano, and J. D. Hogan, "Microstructural and mechanical characterization of variability in porous advanced ceramics using x-ray computed tomography and digital image correlation," *Materials Characterization*, vol. 158, p. 109 929, 2019.

[27] M. Ji, H. Li, J. Zheng, S. Yang, Z. Zaiemyekeh, and J. D. Hogan, "An experimental study on the strain-rate-dependent compressive and tensile response of an alumina ceramic," *Ceramics International*, vol. 48, no. 19, pp. 28 121–28 134, 2022.

[28] P. H. Lin, L. Tsai, and N. Liou, "Dynamic response of alumina ceramics under brazilian disc test conditions," in *Dynamic Behavior of Materials, Volume 1*, Springer, 2018, pp. 31–38.

[29] J. Zheng, M. Ji, Z. Zaiemyekeh, H. Li, and J. D. Hogan, "Strain-rate-dependent compressive and compression-shear response of an alumina ceramic," *Journal of the European Ceramic Society*, 2022.

[30] N. Kawai, T. Kotani, Y. Kakimoto, and E. Sato, “Fracture behavior of silicon nitride ceramics under combined compression–torsion stresses analyzed by multiaxial fracture statistics,” *Journal of the European Ceramic Society*, vol. 31, no. 9, pp. 1827–1833, 2011.

[31] S. Nohut, A. Usbeck, H. Özcoban, D. Krause, and G. A. Schneider, “Determination of the multiaxial failure criteria for alumina ceramics under tension–torsion test,” *Journal of the European Ceramic Society*, vol. 30, no. 16, pp. 3339–3349, 2010.

[32] M. Scapin, L. Peroni, and M. Avalle, “Dynamic brazilian test for mechanical characterization of ceramic ballistic protection,” *Shock and Vibration*, vol. 2017, 2017.

[33] J. Chen, B. Guo, H. Liu, H. Liu, and P. Chen, “Dynamic brazilian test of brittle materials using the split hopkinson pressure bar and digital image correlation,” *Strain*, vol. 50, no. 6, pp. 563–570, 2014.

[34] A. Elghazel, R. Taktak, and J. Bouaziz, “Determination of elastic modulus, tensile strength and fracture toughness of bioceramics using the flattened brazilian disc specimen: Analytical and numerical results,” *Ceramics International*, vol. 41, no. 9, pp. 12 340–12 348, 2015.

[35] N. Erarslan and D. J. Williams, “Experimental, numerical and analytical studies on tensile strength of rocks,” *International Journal of Rock Mechanics and Mining Sciences*, vol. 49, pp. 21–30, 2012.

[36] S. Xu, J. Huang, P. Wang, C. Zhang, L. Zhou, and S. Hu, “Investigation of rock material under combined compression and shear dynamic loading: An experimental technique,” *International Journal of Impact Engineering*, vol. 86, pp. 206–222, 2015.

[37] H. B. Du, F. Dai, Y. Liu, Y. Xu, and M.-d. Wei, “Dynamic response and failure mechanism of hydrostatically pressurized rocks subjected to high loading rate impacting,” *Soil Dynamics and Earthquake Engineering*, vol. 129, p. 105 927, 2020.

[38] C. E. Anderson, P. E. O’Donoghue, J. Lankford, and J. D. Walker, “Numerical simulations of shpb experiments for the dynamic compressive strength and failure of ceramics,” *International journal of fracture*, vol. 55, no. 3, pp. 193–208, 1992.

[39] M. Shafiq and G. Subhash, “An extended mohr–coulomb model for fracture strength of intact brittle materials under ultrahigh pressures,” *Journal of the American Ceramic Society*, vol. 99, no. 2, pp. 627–630, 2016.

[40] Y. Xu and F. Dai, "Dynamic response and failure mechanism of brittle rocks under combined compression-shear loading experiments," *Rock Mechanics and Rock Engineering*, vol. 51, no. 3, pp. 747–764, 2018.

[41] Y. Xu, A. Pellegrino, F. Dai, and H. Du, "Experimental and numerical investigation on the dynamic failure envelope and cracking mechanism of precompressed rock under compression-shear loads," *International Journal of Geomechanics*, vol. 21, no. 11, p. 04 021 208, 2021.

[42] Q. Zhang, F. Dai, and Y. Liu, "Experimental assessment on the dynamic mechanical response of rocks under cyclic coupled compression-shear loading," *International Journal of Mechanical Sciences*, vol. 216, p. 106 970, 2022.

[43] H.-b. Du, F. Dai, Y. Xu, Z. Yan, and M.-d. Wei, "Mechanical responses and failure mechanism of hydrostatically pressurized rocks under combined compression-shear impacting," *International Journal of Mechanical Sciences*, vol. 165, p. 105 219, 2020.

[44] G. Johnson and T. Holmquist, "A computational constitutive model for brittle materials subjected to large strains, high strain rates and high pressures," *Shock wave and high-strain-rate phenomena in materials*, pp. 1075–1081, 1992.

[45] G. R. Johnson and T. J. Holmquist, "An improved computational constitutive model for brittle materials," in *AIP conference proceedings*, American Institute of Physics, vol. 309, 1994, pp. 981–984.

[46] G. R. Johnson, T. J. Holmquist, and S. R. Beissel, "Response of aluminum nitride (including a phase change) to large strains, high strain rates, and high pressures," *Journal of Applied Physics*, vol. 94, no. 3, pp. 1639–1646, 2003.

[47] C. H. M. Simha, S. Bless, and A. Bedford, "Computational modeling of the penetration response of a high-purity ceramic," *International Journal of Impact Engineering*, vol. 27, no. 1, pp. 65–86, 2002.

[48] E. Simons, J. Weerheijm, and L. J. Sluys, "A viscosity regularized plasticity model for ceramics," *European Journal of Mechanics-A/Solids*, vol. 72, pp. 310–328, 2018.

[49] E. Simons, J. Weerheijm, and L. J. Sluys, "Simulating brittle and ductile response of alumina ceramics under dynamic loading," *Engineering Fracture Mechanics*, vol. 216, p. 106 481, 2019.

[50] A. Rajendran, “Modeling the impact behavior of AD85 ceramic under multiaxial loading,” *International Journal of Impact Engineering*, vol. 15, no. 6, pp. 749–768, 1994.

[51] A. Rajendran and D. Grove, “Modeling the shock response of silicon carbide, boron carbide and titanium diboride,” *International Journal of Impact Engineering*, vol. 18, no. 6, pp. 611–631, 1996.

[52] V. Deshpande and A. Evans, “Inelastic deformation and energy dissipation in ceramics: A mechanism-based constitutive model,” *Journal of the Mechanics and Physics of Solids*, vol. 56, no. 10, pp. 3077–3100, 2008.

[53] V. S. Deshpande, E. N. Gamble, B. G. Compton, R. M. McMeeking, A. G. Evans, and F. W. Zok, “A constitutive description of the inelastic response of ceramics,” *Journal of the American Ceramic Society*, vol. 94, s204–s214, 2011.

[54] B. Paliwal, K. Ramesh, and J. McCauley, “Direct observation of the dynamic compressive failure of a transparent polycrystalline ceramic (AlON),” *Journal of the American Ceramic Society*, vol. 89, no. 7, pp. 2128–2133, 2006.

[55] S. Sayahlatifi, C. Shao, A. McDonald, and J. D. Hogan, “3D microstructure-based fe simulation of cold-sprayed Al-Al2O3 composite coatings under indentation and quasi-static compression,” in *ITSC2021*, ASM International, 2021, pp. 386–395.

[56] W. Wang, L. Sluys, and R. De Borst, “Viscoplasticity for instabilities due to strain softening and strain-rate softening,” *International Journal for Numerical Methods in Engineering*, vol. 40, no. 20, pp. 3839–3864, 1997.

[57] E. Simons, J. Weerheijm, G. Toussaint, and L. Sluys, “An experimental and numerical investigation of sphere impact on alumina ceramic,” *International Journal of Impact Engineering*, vol. 145, p. 103 670, 2020.

[58] M. Khan and M. Iqbal, “Failure and fragmentation of ceramic target with varying geometric configuration under ballistic impact,” *Ceramics International*, 2022.

[59] Y. F. Gao, J. Wang, Q. Y. Li, and Y. H. Ding, “Dynamic response behaviours of Al2O3 ceramics with different grain sizes under SHPB compression loading,” in *Key Engineering Materials*, Trans Tech Publ, vol. 922, 2022, pp. 45–51.

[60] W. G. Fahrenholtz, E. J. Wuchina, W. E. Lee, and Y. Zhou, *Ultra-high temperature ceramics: materials for extreme environment applications*. John Wiley & Sons, 2014.

[61] Q.-Z. Wang and L. Xing, "Determination of fracture toughness kic by using the flattened brazilian disk specimen for rocks," *Engineering fracture mechanics*, vol. 64, no. 2, pp. 193–201, 1999.

[62] J. J. Swab, C. S. Meredith, D. T. Casem, and W. R. Gamble, "Static and dynamic compression strength of hot-pressed boron carbide using a dumbbell-shaped specimen," *Journal of Materials Science*, vol. 52, no. 17, pp. 10 073–10 084, 2017.

[63] J. J. Swab, J. Yu, R. Gamble, and S. Kilczewski, "Analysis of the diametral compression method for determining the tensile strength of transparent magnesium aluminate spinel," *International journal of fracture*, vol. 172, no. 2, pp. 187–192, 2011.

[64] H. Lin, W. Xiong, and Q. Yan, "Modified formula for the tensile strength as obtained by the flattened brazilian disk test," *Rock Mechanics and Rock Engineering*, vol. 49, no. 4, pp. 1579–1586, 2016.

[65] A. Griffith, "Proceedings of the first international congress on applied mechanics," *Delft. J. Waltman Jr, Delft*, pp. 55–63, 1924.

[66] B. M. Koch, P. Jannotti, D. Mallick, B. Schuster, T. Sano, and J. D. Hogan, "Influence of microstructure on the impact failure of alumina," *Materials Science and Engineering: A*, vol. 770, p. 138 549, 2020.

[67] C. Lo, H. Li, G. Toussaint, and J. D. Hogan, "On the evaluation of mechanical properties and ballistic performance of two variants of boron carbide," *International Journal of Impact Engineering*, vol. 152, p. 103 846, 2021.

[68] Z. Zaiemyekeh, G. Liaghat, H. Ahmadi, M. Khan, and O. Razmkhah, "Effect of strain rate on deformation behavior of aluminum matrix composites with Al-Al2O3 nanoparticles," *Materials Science and Engineering: A*, vol. 753, pp. 276–284, 2019.

[69] Q. Wang, W. Li, and H. Xie, "Dynamic split tensile test of flattened brazilian disc of rock with shpb setup," *Mechanics of Materials*, vol. 41, no. 3, pp. 252–260, 2009.

[70] Q. Wang, X. Jia, S. Kou, Z. Zhang, and P.-A. Lindqvist, "The flattened brazilian disc specimen used for testing elastic modulus, tensile strength and fracture toughness of brittle rocks: Analytical and numerical results," *International Journal of Rock Mechanics and Mining Sciences*, vol. 41, no. 2, pp. 245–253, 2004.

[71] J. Venkatesan, M. A. Iqbal, and V. Madhu, "Experimental and numerical study of the dynamic response of B_4C ceramic under uniaxial compression," *Thin-Walled Structures*, vol. 154, p. 106 785, 2020.

[72] D. J. Frew, M. J. Forrestal, and W. Chen, "Pulse shaping techniques for testing brittle materials with a split hopkinson pressure bar," *Experimental mechanics*, vol. 42, no. 1, pp. 93–106, 2002.

[73] Z. Rosenberg, N. Brar, and S. Bless, "Dynamic high-pressure properties of aln ceramic as determined by flyer plate impact," *Journal of applied physics*, vol. 70, no. 1, pp. 167–171, 1991.

[74] M. Kipp and D. Grady, "Shock phase transformation and release properties of aluminum nitride," *Le Journal de Physique IV*, vol. 4, no. C8, pp. C8–249, 1994.

[75] M. Chen, J. McCauley, D. Dandekar, and N. Bourne, "Dynamic plasticity and failure of high-purity alumina under shock loading," *Nature materials*, vol. 5, no. 8, pp. 614–618, 2006.

[76] P. Baranowski *et al.*, "Fracture and fragmentation of dolomite rock using the JH2 constitutive model: Parameter determination, experiments and simulations," *International Journal of Impact Engineering*, vol. 140, p. 103 543, 2020.

[77] Y. Zhu, G. Liu, Y. Wen, C. Xu, W. Niu, and G. Wang, "Back-spalling process of an Al2O3 ceramic plate subjected to an impact of steel ball," *International Journal of Impact Engineering*, vol. 122, pp. 451–471, 2018.

[78] G. Subhash, S. Maiti, P. H. Geubelle, and D. Ghosh, "Recent advances in dynamic indentation fracture, impact damage and fragmentation of ceramics," *Journal of the American Ceramic Society*, vol. 91, no. 9, pp. 2777–2791, 2008.

[79] C. Y. Rena, G. Ruiz, and A. Pandolfi, "Numerical investigation on the dynamic behavior of advanced ceramics," *Engineering Fracture Mechanics*, vol. 71, no. 4-6, pp. 897–911, 2004.

[80] M. Z. Sheikh *et al.*, "Static and dynamic brazilian disk tests for mechanical characterization of annealed and chemically strengthened glass," *Ceramics International*, vol. 45, no. 6, pp. 7931–7944, 2019.

[81] ABAQUS, "Simulia. abaqus/cae version 6.14-2 (2014). dassault systèmes simulia corp," *Provid. RI, USA*, 2014.

[82] Q. Li and H. Meng, "About the dynamic strength enhancement of concrete-like materials in a split hopkinson pressure bar test," *International Journal of solids and structures*, vol. 40, no. 2, pp. 343–360, 2003.

[83] S. Nemat-Nasser and M. Obata, "A microcrack model of dilatancy in brittle materials," 1988.

[84] B. M. Koch, C. Lo, T. Sano, and J. D. Hogan, "Bulking as a mechanism in the failure of advanced ceramics," in *Hypervelocity Impact Symposium*, American Society of Mechanical Engineers, vol. 883556, 2019, V001T05A001.

[85] K. J. Stone and D. M. Wood, "Effects of dilatancy and particle size observed in model tests on sand," *Soils and Foundations*, vol. 32, no. 4, pp. 43–57, 1992.

[86] M. Poliotti and J.-M. Bairán, "A new concrete plastic-damage model with an evolutive dilatancy parameter," *Engineering structures*, vol. 189, pp. 541–549, 2019.

[87] D. Warner and J. Molinari, "Micromechanical finite element modeling of compressive fracture in confined alumina ceramic," *Acta Materialia*, vol. 54, no. 19, pp. 5135–5145, 2006.

[88] J. Zhou, A. M. Gokhale, A. Gurumurthy, and S. P. Bhat, "Realistic microstructural rve-based simulations of stress–strain behavior of a dual-phase steel having high martensite volume fraction," *Materials Science and Engineering: A*, vol. 630, pp. 107–115, 2015.

[89] L. Malcher, F. A. Pires, and J. C. De Sá, "An extended gtn model for ductile fracture under high and low stress triaxiality," *International Journal of Plasticity*, vol. 54, pp. 193–228, 2014.

[90] S. Bavdekar and G. Subhash, "Failure mechanisms of ceramics under quasi-static and dynamic loads: Overview," *Handbook of damage mechanics*, pp. 579–607, 2022.

[91] Z. Wang, T. Ren, T. Suo, and A. Manes, "Quasi-static and low-velocity impact biaxial flexural fracture of aluminosilicate glass—an experimental and numerical study," *Thin-Walled Structures*, vol. 165, p. 107 939, 2021.

[92] K. Krishnan, S. Sockalingam, S. Bansal, and S. Rajan, "Numerical simulation of ceramic composite armor subjected to ballistic impact," *Composites Part B: Engineering*, vol. 41, no. 8, pp. 583–593, 2010.

[93] L. Zhang, "Influence of shear stress state on dynamic fracture of a glass ceramic macor," *Ceramics International*, 2022.

[94] S. Tan, X. Yao, S. Long, X. Zhang, and S. Zang, "Static and dynamic strength of soda-lime glass under combined compression-shear loading," *Journal of Non-Crystalline Solids*, vol. 516, pp. 14–25, 2019.

[95] L. Yang, G. Wang, G.-F. Zhao, and L. Shen, "A rate-and pressure-dependent damage-plasticity constitutive model for rock," *International Journal of Rock Mechanics and Mining Sciences*, vol. 133, p. 104 394, 2020.

[96] S. Tan, S. Long, X. Yao, and X. Zhang, "An improved material model for loading-path and strain-rate dependent strength of impacted soda-lime glass plate," *Journal of Materials Research and Technology*, vol. 15, pp. 1905–1919, 2021.

[97] M. D. S. Lucio, S. Kultayeva, and Y.-W. Kim, "Improved mechanical strength and thermal resistance of porous sic ceramics with gradient pore sizes," *Journal of the European Ceramic Society*, 2022.

[98] K. Zheng *et al.*, "Compositional tailoring effect on crystal structure, mechanical and thermal properties of γ-AlON transparent ceramics," *Journal of the European Ceramic Society*, vol. 42, no. 6, pp. 2983–2993, 2022.

[99] Y. Zhou, K. Hirao, Y. Yamauchi, and S. Kanzaki, "Tailoring the mechanical properties of silicon carbide ceramics by modification of the intergranular phase chemistry and microstructure," *Journal of the European Ceramic Society*, vol. 22, no. 14-15, pp. 2689–2696, 2002.

[100] M. Zhang *et al.*, "Improved fracture behavior and mechanical properties of alumina textured ceramics," *Materials Letters*, vol. 221, pp. 252–255, 2018.